ACCEPTED MANUSCRIPT

Physics of Fluids

This is the author's peer reviewed, accepted manuscript. However, the online version of record will be different from this version once it has been copyedited and typeset.
PLEASE CITE THIS ARTICLE AS DOI:10.1063/5.0015162

Wakes of rotorcraft in advancing flight: a large-eddy simulation study

Denis-Gabriel Caprace,[1, a)] Philippe Chatelain,[1, b)] and Grégoire Winckelmans[1, b)]

Institute of Mechanics, Materials and Civil Engineering,

Université catholique de Louvain,

1348 Louvain-la-Neuve, Belgium

(Dated: July 16, 2020)

We perform the large-eddy simulation of the flow past a helicopter rotor to support the investigation of rotorcraft wake characteristics and decay mechanisms. A hybrid Lagrangian–Eulerian Vortex Particle–Mesh method is employed to simulate the wake development, with the blades modeled using immersed lifting lines. The validity of the numerical approach is first evaluated through a comparison of the rotor trim parameters with experimental results. Then, the rotor wake at low, medium and high advance ratios is simulated over up to 30 rotor diameters. The wake generation and roll-up are described (i) qualitatively using rotor polar plots and three-dimensional (3-D) vortex dynamics visualizations; (ii) quantitatively using classical integral diagnostics in cross-sections. The highly 3-D unsteady near wake transitions to a system dominated by two parallel vortices, over a distance that depends on the advance ratio. This process is accelerated by the multiple interactions between successive tip vortices, supporting the generation of self-induced turbulence, and uncovering a mechanism of vorticity alignment along the streamwise axis. The vortices in the far wake are compared to typical aircraft ones, and exhibit less compact cores and faster decaying energy. Finally, we illustrate the loss of time periodicity in the far wake using the power spectral density of the kinetic energy, and the backscattering of energy from high rotor harmonics to lower frequencies, as complementary evidence of the intense vortex interaction activity.

[a)]Electronic mail: Denis-Gabriel.Caprace@uclouvain.be; F.R.S./FNRS Research Fellow.

[b)]These authors contributed equally to the work.

AIP Publishing

ACCEPTED MANUSCRIPT
Physics of Fluids
This is the author's peer reviewed, accepted manuscript. However, the online version of record will be different from this version once it has been copyedited and typeset.
PLEASE CITE THIS ARTICLE AS DOI:10.1063/5.0015162
AIP Publishing

I. INTRODUCTION

As is the case for airplanes, the vortices in the wake of an advancing rotorcraft pose a significant threat to the safety of other flights. Wake vortex encounters indeed constitute catastrophic events, and have led to a growing number of incidents and accidents over the past decades[1,2]. Until now, such occurrences mainly entailed smaller airports where light aircraft are mixed with heavy rotorcraft. The most dangerous situations then imply the wake of rotorcraft which, from the regulation point of view, are submitted to ambiguous separation rules. In the near future, the advent of urban air mobility will exacerbate wake-related issues, as increasingly heavier rotary vehicles are expected to evolve in confined, hence dense airspaces. Ensuring the separation between these rotorcraft and their respective wakes will depend upon one's ability to predict these wakes, therefore also requiring the understanding of the underlying physics. In this context, the assessment of rotorcraft wake hazards and the rationalization of operational air traffic procedures also require essential inputs from in-depth wake analyses. However, in comparison to their fixed-wing counterparts, investigations of rotorcraft wakes are quite scarce.

Unfortunately, the available wake surveys are limited to the near rotor region, ever since the early work by McCroskey[3] and Teager *et al.*[4]. Current available experimental visualization techniques are reviewed by Gardner, Wolf, and Raffel[5]. We mention the remarkable work by Bauknecht, Merz, and Raffel[6] for the visualization of tip vortices on a full-scale helicopter (still limited to the near wake). Far wake numerical investigations are almost nonexistent, at least for helicopter rotors. By essence, conventional free wake methods are inappropriate for far wake predictions due to their inviscid assumption[7,8], and further advanced high-fidelity computational methods must be used. Among very accurate approaches, detached eddy simulation with adaptive mesh resolution effectively captures the near wake of hovering and advancing rotors[9,10], at the cost of tremendously high resolution simulations with fine body-fitted meshes. Slightly more affordable results can be obtained using the immersed boundary method[11,12], which captures the presence of blades and complex geometry bodies on cartesian grids, also optionally with multiresolution. An even coarser (hence computationally cheaper) but effective representation of the rotor consists in replacing the blades by an equivalent body force immersed in the volume. This technique, which was rarely applied to rotorcraft configurations (see e.g. Refs. 13 and 14), is much more popular in the wind energy community for the simulation of wind turbine wakes, where it is known as the Actuator Line Method (ALM)[15–17]. Other CFD methods for wake capturing

usually use the vorticity-velocity form of the Navier-Stokes equation, like the Vorticity Transport Model (VTM) by Brown *et al.*[18] later also adapted by Whitehouse and Boschitsch[19]. The VTM was shown to correctly capture wakes over large distances (yet with a loss of resolution in the distance), and also to produce relatively accurate rotor performance predictions, including for dual-rotor configurations[20]. Similarly, fully Lagrangian solvers were employed for the computation of rotor wakes, with a blade representation using either lifting lines[21] or panel methods[22,23]. Domain decompositions were also developed so as to couple an Eulerian solver for the near body flow computation, and a vortex particle method or equivalent in the far field[24–26].

On a different note, Jimenez-Garcia *et al.*[27] proposed guidelines for separation adapted from classical aircraft metrics, following a recent push for helicopter wake categorization. To the authors' knowledge, however, no published research has ever thoroughly addressed the far wake of rotorcraft with an objective of characterization.

Novel insights into the complex flow dynamics governing the development and the decay of rotorcraft wakes are thus necessary. Following a preliminary study exposed in Ref. 28, the present work is concerned with the thorough description of the related processes, and with the characterization of the far wake. To this end, we exploit simulation results produced by a state-of-the-art Vortex Particle–Mesh (VPM) flow solver. This numerical tool has been extensively used for the simulation of wake flows in the past, including aircraft wakes[29]. The addition of Immersed Lifting Lines (ILL) to the framework recently enabled the accurate Large-Eddy Simulation (LES) of the wakes of horizontal[30] and vertical axis wind turbines[31,32] over unprecedented downstream distances. The originality and the efficiency of the approach rely on the mixed Lagrangian-Eulerian character of the VPM method, guaranteeing low dissipation and dispersion errors, and a high computational efficiency. We here extend the method to capture the blade dynamics inherent to rotorcraft applications, hence supporting the comprehensive simulation of the complete wake roll-up process —from the generation of the complex three-dimensional (3-D) near wake to the establishment of two parallel main wake vortices—, including the associated vortex interactions and instabilities, and the ensuing turbulence.

In this article, we first briefly review the numerical method and we present the improvements that we brought for helicopter rotor modeling (Section II). Then, we investigate advancing flight and we explore simulation results of an isolated four-bladed rotor, based on an experimental set-up. The rotor characteristics are exposed in Section III. We verify the consistency of our approach by comparing the control input settings that we obtain for trimmed flight with experimental data

ACCEPTED MANUSCRIPT
Physics of Fluids
This is the author's peer reviewed, accepted manuscript. However, the online version of record will be different from this version once it has been copyedited and typeset.
PLEASE CITE THIS ARTICLE AS DOI:10.1063/5.0015162
AIP Publishing

ACCEPTED MANUSCRIPT
Physics of Fluids
This is the author's peer reviewed, accepted manuscript. However, the online version of record will be different from this version once it has been copyedited and typeset.
PLEASE CITE THIS ARTICLE AS DOI:10.1063/5.0015162
AIP Publishing

(Section IV). Finally, in Section V, we analyse the wake at three advance ratios, with a focus on: (i) the qualitative description of the vortex dynamics, including the vorticity generation on the rotor disc and its relation to the rotor loads; (ii) the investigation of the processes driving the transition from the highly 3-dimensional vortical region in the near wake to a turbulent far wake dominated by two wake vortices, and; (iii) the quantitative characterization of the far wake 2-vortex system (2-VS) in the time and frequency domains.

II. NUMERICAL METHOD

A. Flow solver

The VPM method relies on the vorticity–velocity ($\boldsymbol{\omega} - \mathbf{u}$) formulation of the Navier-Stokes equations for incompressible flows ($\nabla \cdot \mathbf{u} = 0$),

$$\frac{D\boldsymbol{\omega}}{Dt} = (\nabla \mathbf{u}) \cdot \boldsymbol{\omega} + \nu \nabla^2 \boldsymbol{\omega} + \nabla \cdot \mathbf{T}^M \,, \tag{1}$$

where $\frac{D}{Dt} = \frac{\partial}{\partial t} + \mathbf{u} \cdot \nabla$ denotes the Lagrangian derivative, ν is the kinematic viscosity, and $\mathbf{T}^M$ is the sub-grid scales (SGS) model enabling Large-Eddy Simulation. Hence, $\mathbf{u}$ stands for the truncated velocity field, as captured by the LES grid. Using a Helmholtz decomposition of the velocity field $\mathbf{u} = \mathbf{U}_\infty + \mathbf{u}_\omega$, one recovers $\mathbf{u}_\omega$ from the vorticity through the resolution of the Poisson equation

$$\nabla^2 \mathbf{u}_\omega = -\nabla \times \boldsymbol{\omega} \,. \tag{2}$$

Details on the dedicated elliptical solver are given in the next section.

The flow is discretized using a set of Lagrangian particles characterized by a position $\mathbf{x}_p$, a volume V_p and a strength $\boldsymbol{\alpha}_p = \int_{V_p} \boldsymbol{\omega} \, d\mathbf{x}$. The evolution of their position and strength is recovered from the resolution of the following ODEs,

$$\frac{d\mathbf{x}_p}{dt} = \mathbf{u}(\mathbf{x}_p) \,, \tag{3}$$

$$\frac{d\boldsymbol{\alpha}_p}{dt} = \int_{V_p} \left((\boldsymbol{\omega} \cdot \nabla)\mathbf{u} + \nu \nabla^2 \boldsymbol{\omega} + \nabla \cdot \mathbf{T}^M \right) d\mathbf{x} \,, \tag{4}$$

which are here integrated using a third order Runge-Kutta scheme. The spatial differential operators (right-hand-side of Eq. (4)) are computed using finite differences, thus on an underlying

Eulerian grid. Similarly, the turbulence SGS model is implemented as in Ref. 33. High order interpolation schemes are used to recover information back and forth between the particles and the mesh. Other improvements of the VPM method include the periodical operations of remeshing and reprojection. The former prevents particles to deplete some regions of the flow or cluster in others, while the latter maintain the solenoidal property of the vorticity field, which is otherwise not directly enforced by the solver. We refer to the seminal reviews by Cottet and Koumoutsakos [34], Winckelmans [35] for further details on the VPM method. Additionally, Chatelain *et al.* [36] provide a thorough description of the present implementation on massively parallel architectures (here based on the open-source PPM library[37]). Overall, this hybrid framework provides low dispersion and dissipation errors, and also waives the classical CFL condition, thus allowing for large time steps.

B. Poisson solver

The Poisson solver for the velocity exploits the Eulerian formulation based on a uniform cartesian grid, and operates in Fourier space. Advantageously, the related numerical technique (which maintains second order in space) benefits from a computationally efficient 3-D fast Fourier transform algorithm. Originally implemented by Chatelain and Koumoutsakos [38], the solver was recently enhanced and refactored into a dedicated software library called *FLUPS*[39]. Importantly, it now accomodates the simultaneous definition of periodic, unbounded, semi-unbounded, inlet and outlet boundaries.

Typically, inflow and outflow conditions are obtained by imposing symmetries on $\mathbf{u}_\omega$ (and correspondingly on $\boldsymbol{\omega}$). For instance, the outflow in the wake of a lifting body (such as the present rotor) assumes an even parity for the vorticity component normal to the boundary, and an odd parity for the tangential components. The wake vortices thus connect normally to the outflow plane. At the inflow, the same parities are imposed so that the absolute velocity normal to the inflow plane is uniform and equal to a predefined U_∞.

C. Blade modeling

The rotor blade coarse scale aerodynamics are accounted for through an Immersed Lifting Line (ILL) method[30], recently validated and improved[40]. This technique presents strong similarities

ACCEPTED MANUSCRIPT
Physics of Fluids
This is the author's peer reviewed, accepted manuscript. However, the online version of record will be different from this version once it has been copyedited and typeset.
PLEASE CITE THIS ARTICLE AS DOI:10.1063/5.0015162
AIP Publishing

ACCEPTED MANUSCRIPT
Physics of Fluids
This is the author's peer reviewed, accepted manuscript. However, the online version of record will be different from this version once it has been copyedited and typeset.
PLEASE CITE THIS ARTICLE AS DOI:10.1063/5.0015162
AIP Publishing

with the ALM, except that it is fully compatible with the Lagrangian character of the VPM method. The ILL readily takes care of the generation of vorticity, instead of applying a force in a volume.

Based on the instantaneous velocity and angle of attack of every blade segment, a third generation Leishman-Beddoes Dynamic Stall (DS) model (summarized in Ref. 41) is used to determine the lift and drag forces produced by the airfoil, thus aiming at a better (yet simplified) representation of the complex unsteady aerodynamics. Indeed, a series of indicial functions account for delays in the development of the lift and drag on the airfoil. The influence of leading edge vortex shedding is also modeled. Such events are assumed to occur as soon as a prescribed value of the normal force coefficient is exceeded.

Using the so-obtained lift, the circulation around the local 2D airfoil is recovered from the Kutta-Joukowski theorem,

$$\mathbf{l} = \rho \mathbf{U}_{\text{rel}} \times \mathbf{\Gamma} \,, \tag{5}$$

where $\mathbf{l}$ is the lift per unit span of the segment, $\mathbf{U}_{\text{rel}}$ is the relative flow velocity and $\mathbf{\Gamma}$ is the circulation vector (along the blade span). In the flow, the blade segments are then represented by a set of equivalent bound vorticity particles, accounting for a mollification (i.e. a small spatial spreading, of the order of the mesh size h, in the direction of $\mathbf{l}$) required for numerical purposes. The shed vorticity, which is deduced from the time and space variation of the bound vorticity, is released in the bulk flow through new vorticity carrying particles (also with mollification) and then merged with the pre-existing flow particles.

Considering the sharp rectangular shape of rotor blades, we introduce a numerical smoothing of the tip. In practice, the blade chord is brought to 0 over two computational cells, thus slightly modifying the chord distribution with a length c at $R-h$, $c/2$ at R, and 0 at $R+h$; where h is the mesh size. This helps mitigate the effect of the mollified vorticity field (and the consequence on the measured downwash/induction), which otherwise gives rise to spuriously high loads at the very tip of the blade[42,43].

D. Blade dynamics

The rigid blade flapping motion is captured through a two-way coupling of the flow solver with the multi-body integrator ROBOTRAN[44]. The latter uses symbolic generation to establish the equations of the direct dynamics of a model. This approach enables the efficient solving of the dynamics of complex multi-body systems such as the complete mechanism of a rotor hub,

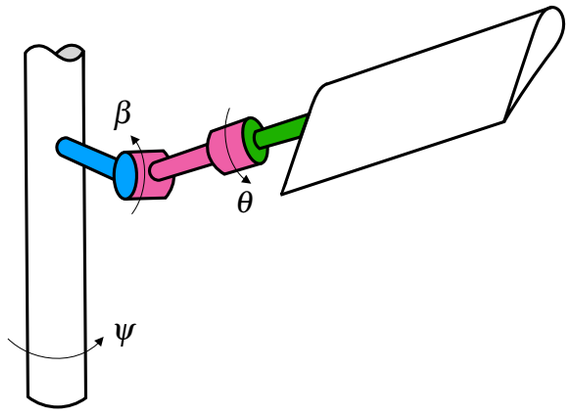


Figure 1. Simplified kinematics of one blade

provided that the blade aerodynamic forces can be recovered from the flow solver. In the present loosely coupled implementation, ROBOTRAN and the VPM solver use separate time integrators which communicate to advance the global state of the simulation consistently. Practically, the aerodynamic forces computed by the lifting lines are sent to ROBOTRAN at each sub-step of the flow solver. The equations of motion for the rigid blades are integrated by the multi-body solver over the sub-step and the resulting positions of the lifting bodies are then updated in the flow simulation. The procedure is repeated at every sub-step of the simulation which captures the influence of the flow on the blades, and vice versa.

In this study, a rather simple rotor model is used, as shown in Fig. 1. It consists of a rotor shaft rotating at a prescribed angular velocity. The blades, which are connected to the shaft with a given hinge offset, have two degrees of freedom, respectively for flapping (β) and pitching (θ). Following the rotorcraft convention, the blade pitching motion is prescribed as

$$\theta(\psi) = \theta_0 + \theta_{1s}\sin\psi + \theta_{1c}\cos\psi, \tag{6}$$

where ψ is the revolution angle (equal to 0 when the blade points backwards). A closed loop controller directs the cyclic controls (θ_{1c} and θ_{1s}) in order to cancel the pitching and rolling moments of the rotor measured at the hub center. The collective (θ_0) can also be dynamically adapted to maintain a given thrust coefficient C_T for the rotor. The aerodynamic and inertial efforts applying on each blade thus result in the the proper time variation of their flapping angle β.

ACCEPTED MANUSCRIPT
Physics of Fluids
This is the author's peer reviewed, accepted manuscript. However, the online version of record will be different from this version once it has been copyedited and typeset.
PLEASE CITE THIS ARTICLE AS DOI:10.1063/5.0015162
AIP Publishing

ACCEPTED MANUSCRIPT
Physics of Fluids
This is the author's peer reviewed, accepted manuscript. However, the online version of record will be different from this version once it has been copyedited and typeset.
PLEASE CITE THIS ARTICLE AS DOI:10.1063/5.0015162
AIP Publishing

III. ROTOR CONFIGURATION

The rotor considered here reproduces the experimental set-up by Berry and Chopra[45], and Bowen-Davies[46] who studied an articulated four-bladed rotor under moderate to very high advance ratios, and for various tilt angles of the rotor shaft. The rotor and blade properties are summarized in Table I. The blades are assumed rigid, untwisted and unswept.

Table I. Rotor and blade properties from Ref. 46.

Rotor radius, $R\,[m]$	0.849
Blade chord, $c\,[m]$	0.080
Solidity, s	0.120
Airfoil	NACA0012
Hinge offset, $[\%R]$	6.3%
Root cut-out, $R_i\,[\%R]$	22.5%
Center of mass, $[\%R]$	61.3%
Twist	untwisted
Sweep	unswept
Blade mass density, $m_0\,[kg/m]$	0.347
Flap inertia[a], $I_\beta\,[kg\,m^2]$	0.034

[a] from center of mass.

The rotor angular velocity could be varied in the experiment. We select $\Omega = 600\,[\mathrm{RPM}]$, which corresponds to a blade tip Reynolds number of $Re_c = 4\,10^5$. The inflow velocity in the simulation will be adjusted to obtain three advance ratios: $\mu = \frac{U_\infty}{\Omega R} = 0.08$, 0.25 and 0.41. These values correspond to a conventional helicopter respectively in a low, a moderate and a high speed advancing flight.

We use the aerodynamic polars from Lind and Jones[47] to tune the static coefficients of the DS model. The result of the curve fitting is presented in Fig. 2. On the other hand, the standard values are used for the coefficients related to the dynamics (summarized in Ref. 41).

We focus on two specific geometries for our simulations. The first one, for which we present the results in Section IV, has a rotor shaft which is perpendicular to the free stream velocity ($\alpha_s = 0^\circ$). The corresponding results will be compared to experimental data. The second geometry has the main rotor shaft tilted forward (nose down, $\alpha_s = 4^\circ$) to mimic the attitude of an advancing rotorcraft. This configuration was not tested in the experiments, where backward tilting was investigated instead. The corresponding results are presented in Section V.

We use inflow and outflow BCs as defined in Section II B and unbounded boundaries on the

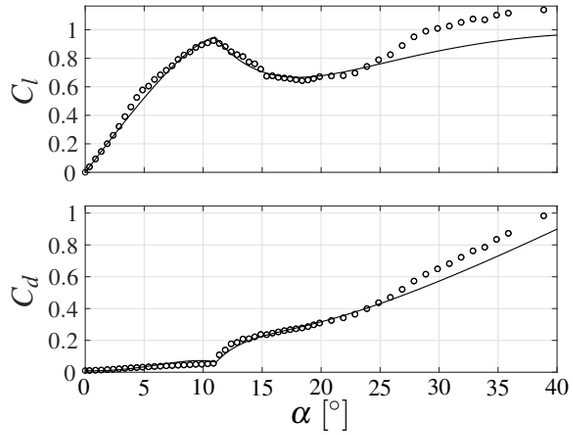


Figure 2. Sectional lift and drag coefficients of the NACA0012 airfoil at $\mathrm{Re} = 3.3\,10^5$: experimental data from Ref. 47 (∘) and fit of the static part of the dynamic stall model (—).

side of the computational domain. The rotor center is located at $1.5D$ of the inflow plane. The rotor hub is here not accounted for.

IV. ROTOR TRIM VERIFICATION

A first set of short-domain simulations is performed as a verification of our numerical model against the experiment. Simulations are run for pre-set values of the collective control θ_0. The cyclic controls θ_{1c} and θ_{1s} are adapted in order to trim the rotor by cancelling the pitching and rolling moments at the hub. Two spatial resolutions are investigated: a coarse configuration (48 particles per D) and a fine configuration (128 particles per D).

In Fig. 3, we compare the thrust coefficient $C_T = \frac{T}{\frac{1}{2}\rho(\Omega R)^2 \mathcal{S}}$ and the cyclic control angles θ_{1c} and θ_{1s} for trim with experimental data, at the available μ (medium and high). Notice that T is the force in the direction of the rotor shaft, and $\mathcal{S} = \pi R^2$. Results from the University of Maryland Advanced Rotorcraft Code (UMARC) are also presented. This model uses a flexible beam representation of the blades coupled to a lifting line free wake approach for the aerodynamics[48].

The slope of the thrust coefficient is overestimated by our lifting lines. This behavior could be expected from previous results on other rotary configurations such as wind turbines[30,32], where the ILL systematically predicts higher loads. Consistently, a similar trend is generally observed with the actuator line model, as reported in Refs. 43 and 49 (among others). The origin of this discrepancy is traced back to a mismatch in the tip loads caused by the mollification inherent to the lines[42]. The induced velocity at the tip of the blades drops, hence increasing the angle of attack

ACCEPTED MANUSCRIPT
Physics of Fluids
This is the author's peer reviewed, accepted manuscript. However, the online version of record will be different from this version once it has been copyedited and typeset.
PLEASE CITE THIS ARTICLE AS DOI:10.1063/5.0015162
AIP Publishing

ACCEPTED MANUSCRIPT
Physics of Fluids
This is the author's peer reviewed, accepted manuscript. However, the online version of record will be different from this version once it has been copyedited and typeset.
PLEASE CITE THIS ARTICLE AS DOI:10.1063/5.0015162
AIP Publishing

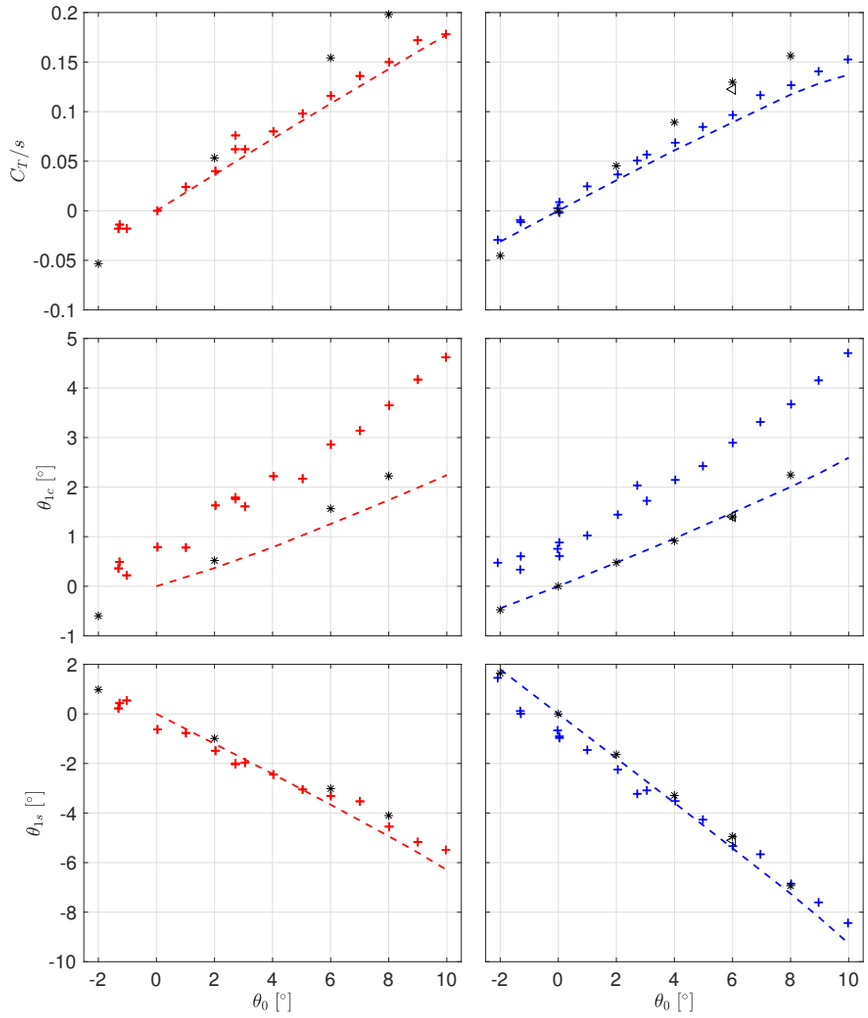


Figure 3. Thrust coefficient, lateral and longitudinal trim settings for various angles of the collective and for a rotor mast at $\alpha_s = 0°$ for $\mu = 0.25$ (left) and $\mu = 0.41$ (right), obtained with VPM at coarse ($*$) and high resolution ($\triangleleft$), compared to experimental results ($+$) and UMARC simulations (- -)[46].

in that region. For rotary wings, this results in a higher predicted thrust and a lower torque (due to the tilting of the local lift vector). The refined case at $\mu = 0.41$ gets closer to the experimental solution, still with a noticeable discrepancy.

However, the slope of the lateral cyclic (θ_{1c}) for trim is in fairly good agreement with the experiment. The offset is explained by an interaction between the wake of the hub/mast, and the blades. This interaction is not captured in our numerical simulation (neither is it in the UMARC model). The longitudinal cyclic (θ_{1s}) also agrees well with the experimental results and with the UMARC model, for both advance ratios.

Overall, our numerical model of the rotor yields satisfactory agreement with experimental data,

ACCEPTED MANUSCRIPT
Physics of Fluids
This is the author's peer reviewed, accepted manuscript. However, the online version of record will be different from this version once it has been copyedited and typeset.
PLEASE CITE THIS ARTICLE AS DOI:10.1063/5.0015162
AIP Publishing

Table II. Rotor conditions for the simulations with $\alpha_s = 4°$.

μ	C_T	C_L	θ_0 [°]	θ_{1c} [°]	θ_{1s} [°]
0.08	0.015	2.338	7.34	1.22	–1.14
0.25	0.015	0.239	6.47	0.78	–3.074
0.41	0.015	0.089	8.96	1.00	–6.747

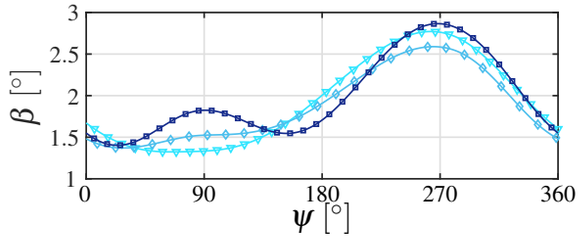


Figure 4. Flapping response of the blades in trimmed flight for $\mu = 0.08$ ( ), 0.25 ( ) and 0.41 ( ).

and we hence proceed with the analysis of the wake.

V. WAKE ANALYSIS OF THE ADVANCING ROTOR

A. Rotor aerodynamics and shed vorticity

From this point on, and for the remainder of this chapter, we consider the rotor geometry with a shaft angle tilted forward by 4°. The spatial development of its wake is computed in simulations with a computational domain length extended to $32D$ (limited to $8D$ for the low advance ratio case). The same resolution is employed for all numerical setups: 128 particles per rotor diameter.

The results presented below are obtained from simulations run on 2048 processors for $\mathcal{O}(24)$ hours. Each simulation was first advanced over 1 convective time ($T_c = L/U_\infty = 32D/U_\infty$) and then continued for the duration of 10 rotor revolutions. These simulations capture the complex transition from the near wake to a fully developed turbulent far wake.

Once again, the cyclic controls θ_{1c} and θ_{1s} are adapted in order to trim the rotor by cancelling the pitching and rolling moments at the hub. The collective is here also adapted in order to maintain a constant value of $C_T = 0.015$. The corresponding conditions are summarized in Table II. The flapping angle of the blades over one revolution is also shown in Fig. 4.

ACCEPTED MANUSCRIPT
Physics of Fluids
This is the author's peer reviewed, accepted manuscript. However, the online version of record will be different from this version once it has been copyedited and typeset.
PLEASE CITE THIS ARTICLE AS DOI:10.1063/5.0015162
AIP Publishing

1. *Rotor aerodynamics and loading*

First, we focus on the rotor operating conditions and on the near wake development for the medium and high advance ratios. Obviously, the vorticity forming the early state of the wake strongly reflects the periodic sollicitations undergone by the rotor blades. The polar representation of the angle of attack (AoA), the lift distribution (C_l^*), and the blade circulation distribution (Γ) on the rotor disk (see Fig. 5) will help shed some light on the vorticity generation mechanism in the near wake.

The mean lift coefficient C_L experienced by all blades over one revolution is here defined as

$$C_L = \frac{1}{2\pi}\int_0^{2\pi}\left(\int_{R_i}^{R}\frac{l(r,\psi)}{\frac{1}{2}\rho U_\infty^2 \mathcal{S}}\,dr\right)d\psi\,, \tag{7}$$

where l is the lift per unit span of the lifting line, and $\mathcal{S} = \pi R^2$. For the sake of clear polar presentation, we define

$$C_l^*(r,\psi) = \frac{1}{2\pi r}\frac{l(r,\psi)}{\frac{1}{2}\rho U_\infty^2}\,. \tag{8}$$

As a result, C_L is obtained by a polar integration of C_l^*,

$$C_L = \frac{1}{\mathcal{S}}\int_0^{2\pi}\left(\int_{R_i}^{R} C_l^*(r,\psi)\,r\,dr\right)d\psi\,. \tag{9}$$

The lift coefficients of the rotor in the conditions studied here are tabulated in Table II.

Clearly visible on the lift polar plot are the Blade Vortex Interactions (BVI) on the advancing side. The first, upstream-most interaction divides the rotor into two regions: a fore region with high loadings and an aft region with lower loadings. This is even more noticeable with $\mu = 0.25$ as the path of the interaction spans the entire disk. The strong radial gradient denotes a transfer of circulation between the bound vortex and the interacting tip vortex. It further suggests that this first BVI dramatically reduces the intensity of the tip vortex that the blade crosses (as observed by Wittmer *et al.*[50] and Garmann and Visbal[51] during perpendicular BVI). Subsequent BVIs appear to be weaker as the blade-vortex offset distance increases due to induced velocities. Their spacing is larger at $\mu = 0.41$, as expected. The lift hence appears to be mainly produced in the fore part of the rotor, and in the aft part where the blades are less subjected to interactions because they pass above the tip vortex paths.

ACCEPTED MANUSCRIPT
Physics of Fluids
This is the author's peer reviewed, accepted manuscript. However, the online version of record will be different from this version once it has been copyedited and typeset.
PLEASE CITE THIS ARTICLE AS DOI:10.1063/5.0015162
AIP Publishing

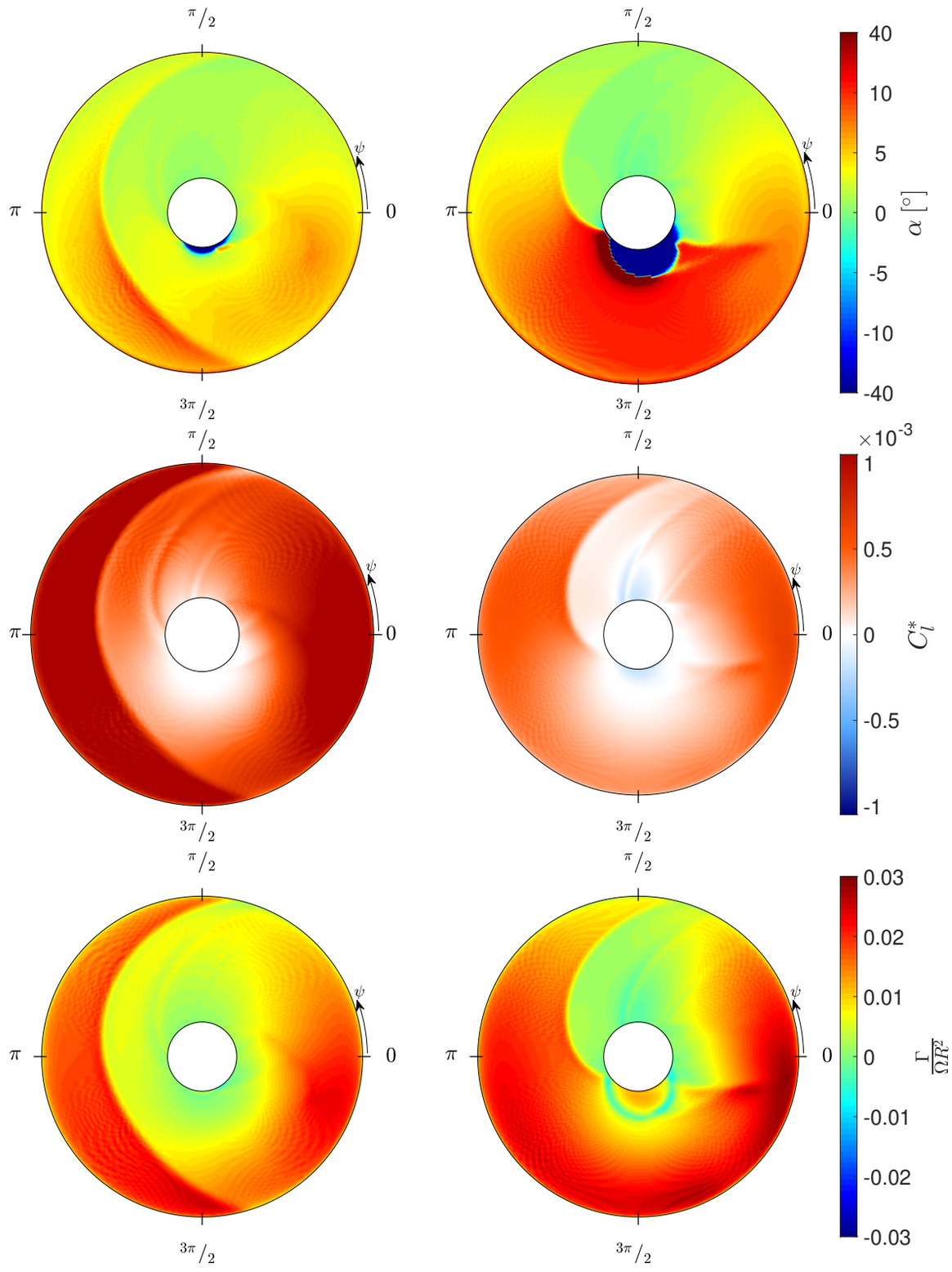


Figure 5. Distribution of angle of attack (top), C_l^* coefficient (center), and blade circulation (bottom) over one rotor revolution, for $\mu = 0.25$ (left) and $\mu = 0.41$ (right). $\boldsymbol{U}_\infty$ from the left.

On the retreating side, the blades experience a more homogeneous loading than on the advancing side: at high advance ratio, BVI is absent. Close to the hub, a sudden AoA increase is visible followed by a sharp drop in the reverse flow region. The circulation and lift respond rather smoothly in that region, indicating that dynamic stall might occur with a limited severity (at least as handled by the present model). It is clear that the aerodynamics in that region features dynamic effects; hence, our predictions strongly depend on the Dynamic Stall model. Due to the proximity to the center of revolution, we expect a limited impact of the DS model on the trim parameters. On the other hand, the circulation is affected and the strong shedding events triggered by sudden circulation changes might be more sensitive to the DS model behavior, especially at high advance ratio.

On average, the blade circulation has a higher value on the retreating side; this is to be correlated with a combination of smaller blade relative velocities and a roughly similar lift production. The strong circulation gradient in the outboard part of the disk hints at more intense tip vortices than those produced on the advancing side. From the polar plot of Γ, one can identify two types of features being shed in the near wake:

- at a certain azimuth, the vorticity shed from the spanwise variation of the blade circulation. The tip vortices best exemplify this type of shedding mechanism, as they result from the sharp drop in circulation at the tip;
- at a certain radius, the vorticity shed due to the temporal variation of the circulation. Dynamic stall, and more generally any rapid variation of the circulation will be the source of a shed vortex.

The so-generated vortical structures then roll up in the near wake.

2. Qualitative description of the roll-up

Figs. 6, 7, 8 show a 3D vorticity visualization by volume rendering of the wakes. At low advance ratio, parallel coherent wake vortices form readily in the very near wake, and the remainder of the tip vortices wraps around them which then break down into turbulence. At higher advances, it takes longer for coherent wake vortices to appear. Figs. 9, 10 present the whole extent of the wakes at medium and high μ from the top, cut in three panels. The "young" blade tip vortices are travelling on cycloidal paths, but are strongly disturbed by BVI and vortex-vortex interactions. As

ACCEPTED MANUSCRIPT
Physics of Fluids
This is the author's peer reviewed, accepted manuscript. However, the online version of record will be different from this version once it has been copyedited and typeset.
PLEASE CITE THIS ARTICLE AS DOI:10.1063/5.0015162
AIP Publishing

ACCEPTED MANUSCRIPT
Physics of Fluids
This is the author's peer reviewed, accepted manuscript. However, the online version of record will be different from this version once it has been copyedited and typeset.
PLEASE CITE THIS ARTICLE AS DOI:10.1063/5.0015162
AIP Publishing

expected, tip vortices are more intense on the retreating side than on the advancing side. However, vortex mergers occur on the advancing side, which lead to an emerging, intense wake vortex; on the other side, reconnection events of the successive tip vortices also finally produce a single flow-aligned vortex. As a result, a globally dominating two-vortex system (2-VS) eventually emerges and governs the wake roll-up, with wake vortex cores apparently in a helical shape.

The merging and reconnection operations are also propitious to the generation of turbulence. In the inboard part of the wake, we observe crossing transverse structures originating in the blade tip vortices shed in the fore and aft part of the revolution. These opposite sign and different intensity vortices interact with each other to create smaller structures. They are also subject to stretching under the influence of the forming 2-VS. These conditions finally lead to the transition to turbulence.

At high advance ratio, the vortical structures shed from the reverse flow region of the rotor also travel along the wake, and strongly interact with the nearby tip vortices produced during the aft part of the revolution. These disturbances propagates and contribute to a rapid development of turbulence, as well.

The hub wake region should also be largely affected by the wake generated by the hub itself, which is not represented here. It was recently observed by Reich, Willits, and Schmitz[52] that velocity in that region bears high harmonics of the rotor revolution frequency, from which we can expect the rapid development of a whole turbulent spectrum. The body wake behind the fuselage and the tail rotor are also important sources of turbulence which would further accelerate the transition and the homogenization of the wake.

B. Forces and moments as recovered from wake quantities

As a first series of diagnostics, we focus on the lift and drag signatures left by the rotor in the wake. Classically, since the far wake is made of two parallel wake vortices, the lift can be obtained as

$$\frac{L}{\rho} = U_\infty \Gamma_0 b_0, \tag{10}$$

AIP Publishing
Physics of Fluids
ACCEPTED MANUSCRIPT
This is the author's peer reviewed, accepted manuscript. However, the online version of record will be different from this version once it has been copyedited and typeset.
PLEASE CITE THIS ARTICLE AS DOI: 10.1063/5.0015162

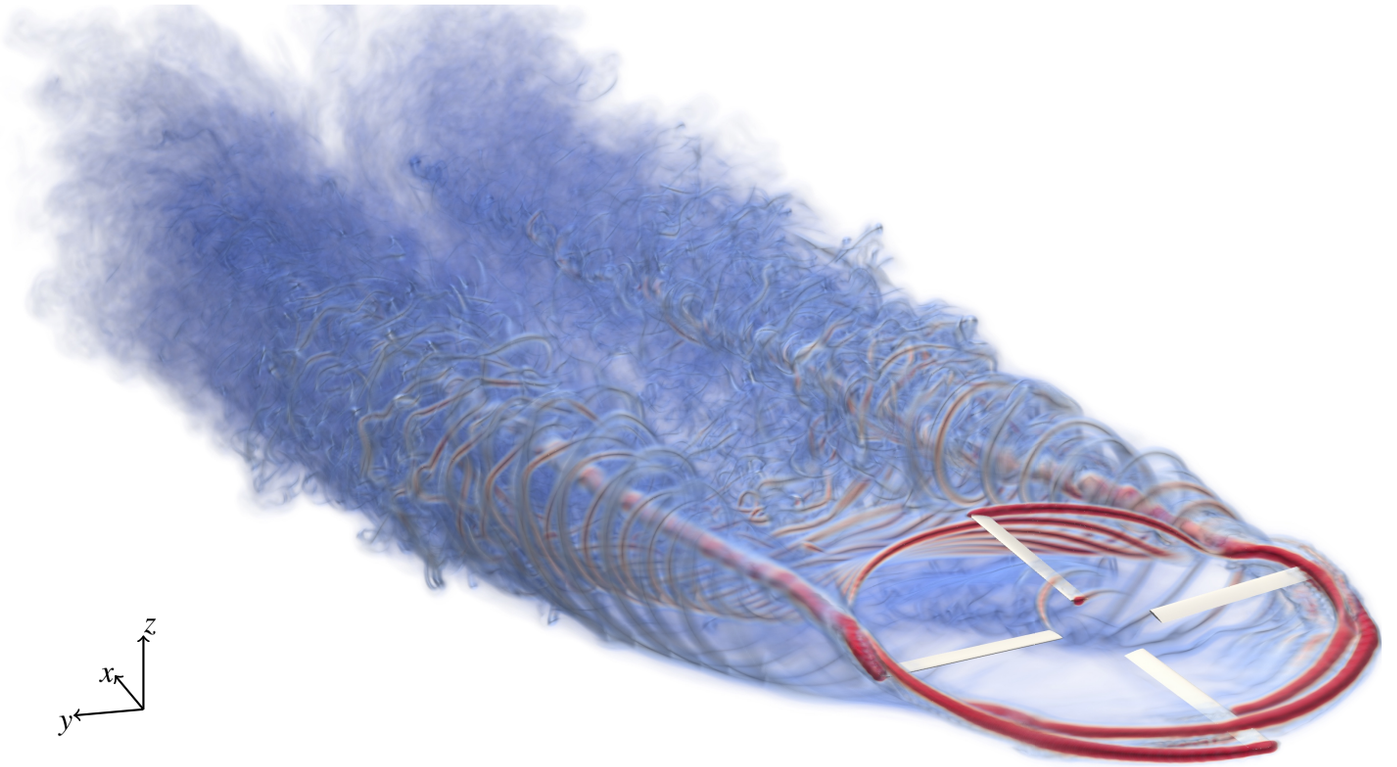


Figure 6. Volume rendering of the vorticity magnitude in the wake of the four-bladed rotor flying at $\mu = 0.08$, over 6 rotor diameters. (Multimedia view)

AIP Publishing Physics of Fluids ACCEPTED MANUSCRIPT

This is the author's peer reviewed, accepted manuscript. However, the online version of record will be different from this version once it has been copyedited and typeset.
PLEASE CITE THIS ARTICLE AS DOI: 10.1063/5.0015162

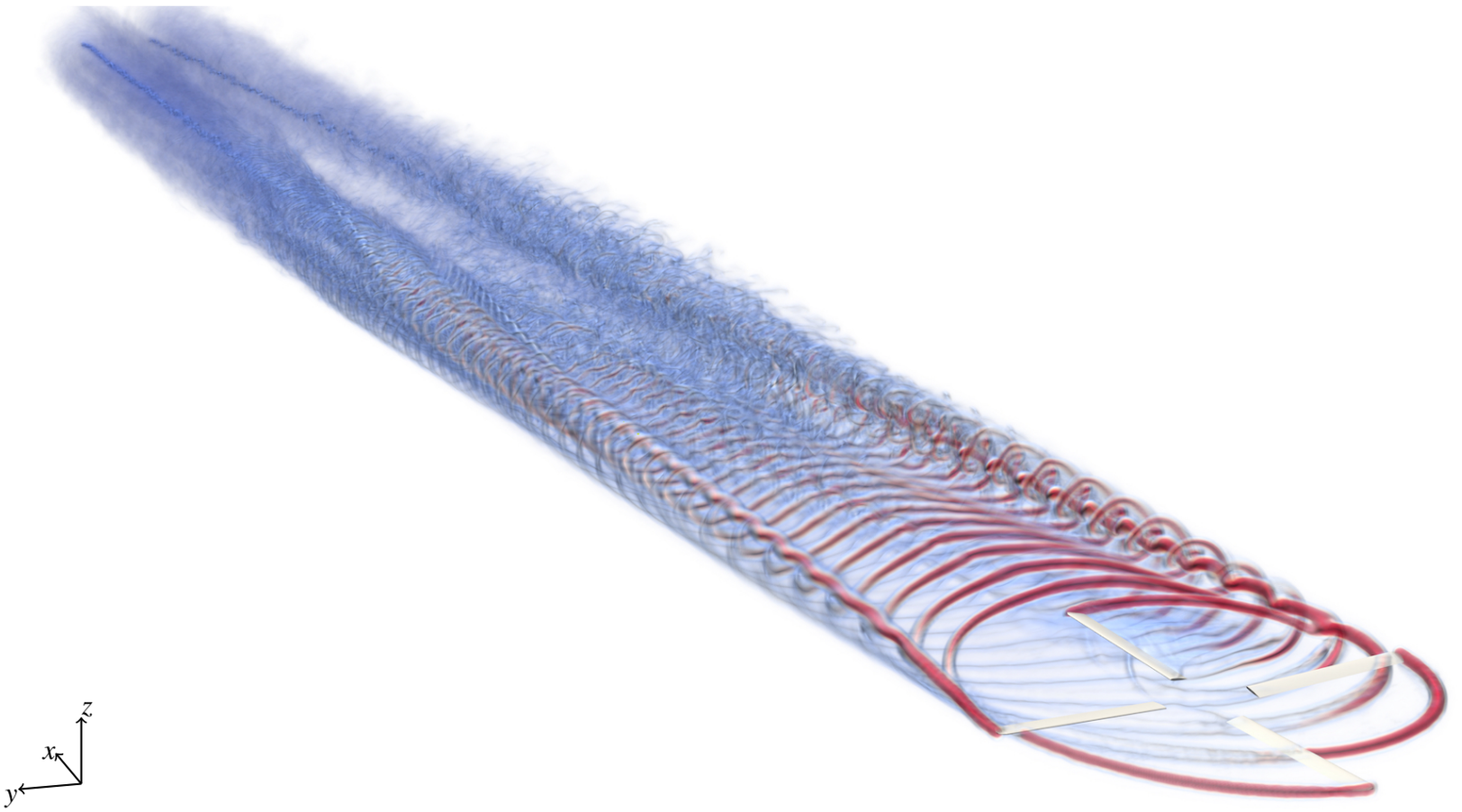


Figure 7. Volume rendering of the vorticity magnitude in the wake of the four-bladed rotor flying at $\mu = 0.25$, over 30 rotor diameters. (Multimedia view)

AIP Publishing
Physics of Fluids
ACCEPTED MANUSCRIPT
This is the author's peer reviewed, accepted manuscript. However, the online version of record will be different from this version once it has been copyedited and typeset.
PLEASE CITE THIS ARTICLE AS DOI: 10.1063/5.0015162

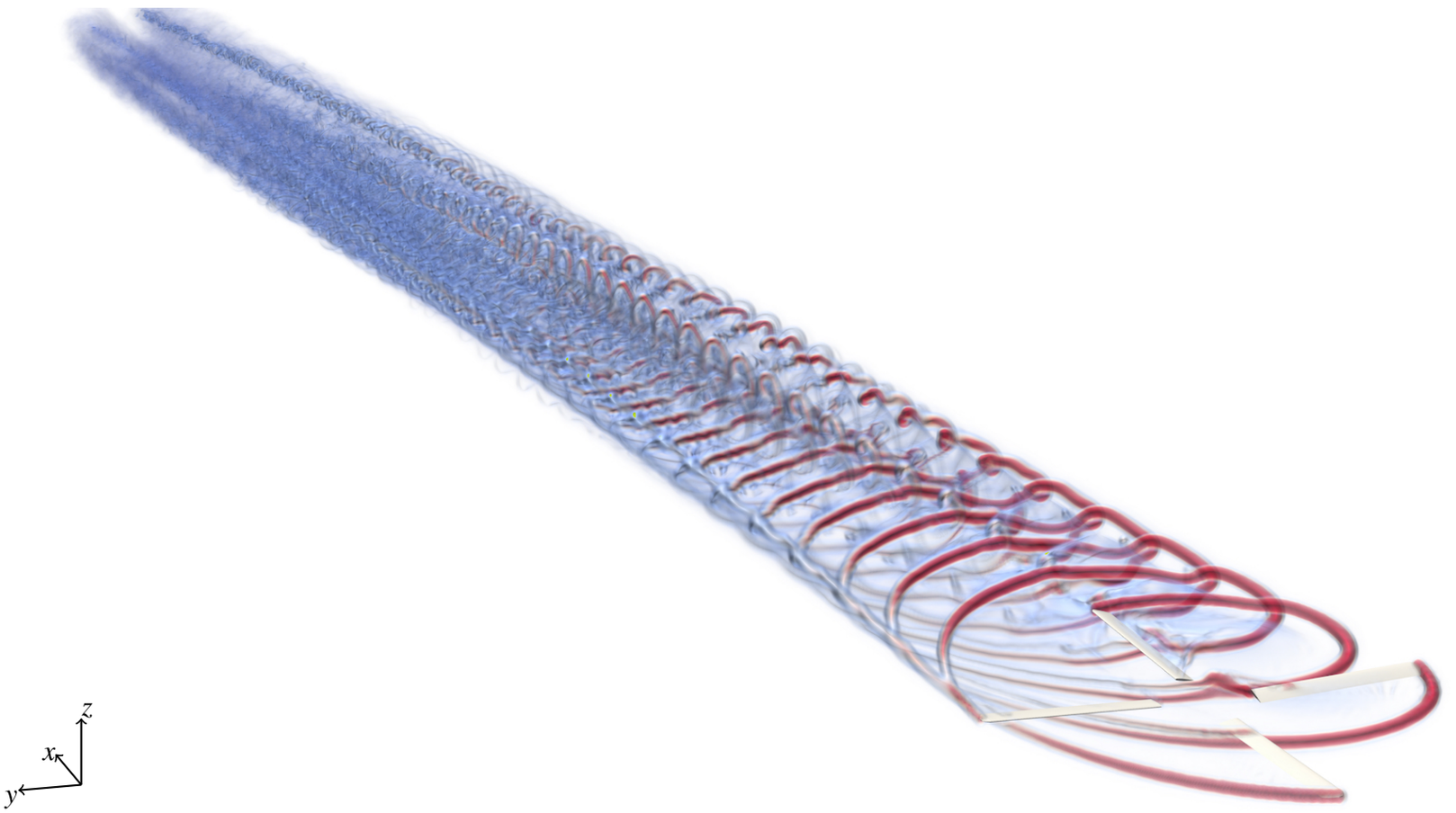


Figure 8. Volume rendering of the vorticity magnitude in the wake of the four-bladed rotor flying at $\mu = 0.41$, over 30 rotor diameters. (Multimedia view)

Physics of Fluids ACCEPTED MANUSCRIPT
This is the author's peer reviewed, accepted manuscript. However, the online version of record will be different from this version once it has been copyedited and typeset.
PLEASE CITE THIS ARTICLE AS DOI:10.1063/5.0015162
AIP Publishing

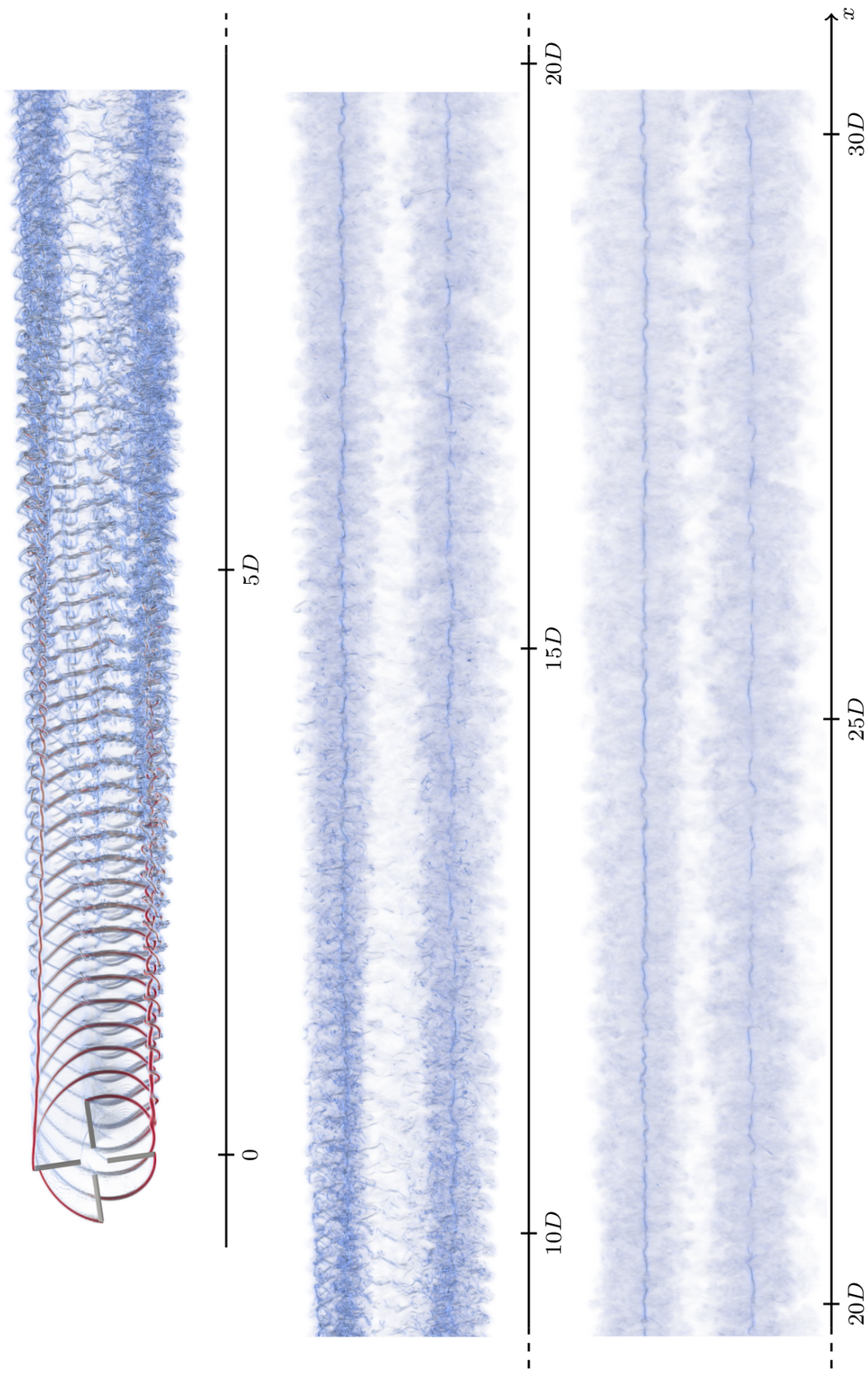


Figure 9. Top view of the near to far wake of the rotor at $\mu = 0.25$.

Physics of Fluids ACCEPTED MANUSCRIPT
This is the author's peer reviewed, accepted manuscript. However, the online version of record will be different from this version once it has been copyedited and typeset.
PLEASE CITE THIS ARTICLE AS DOI:10.1063/5.0015162
AIP Publishing

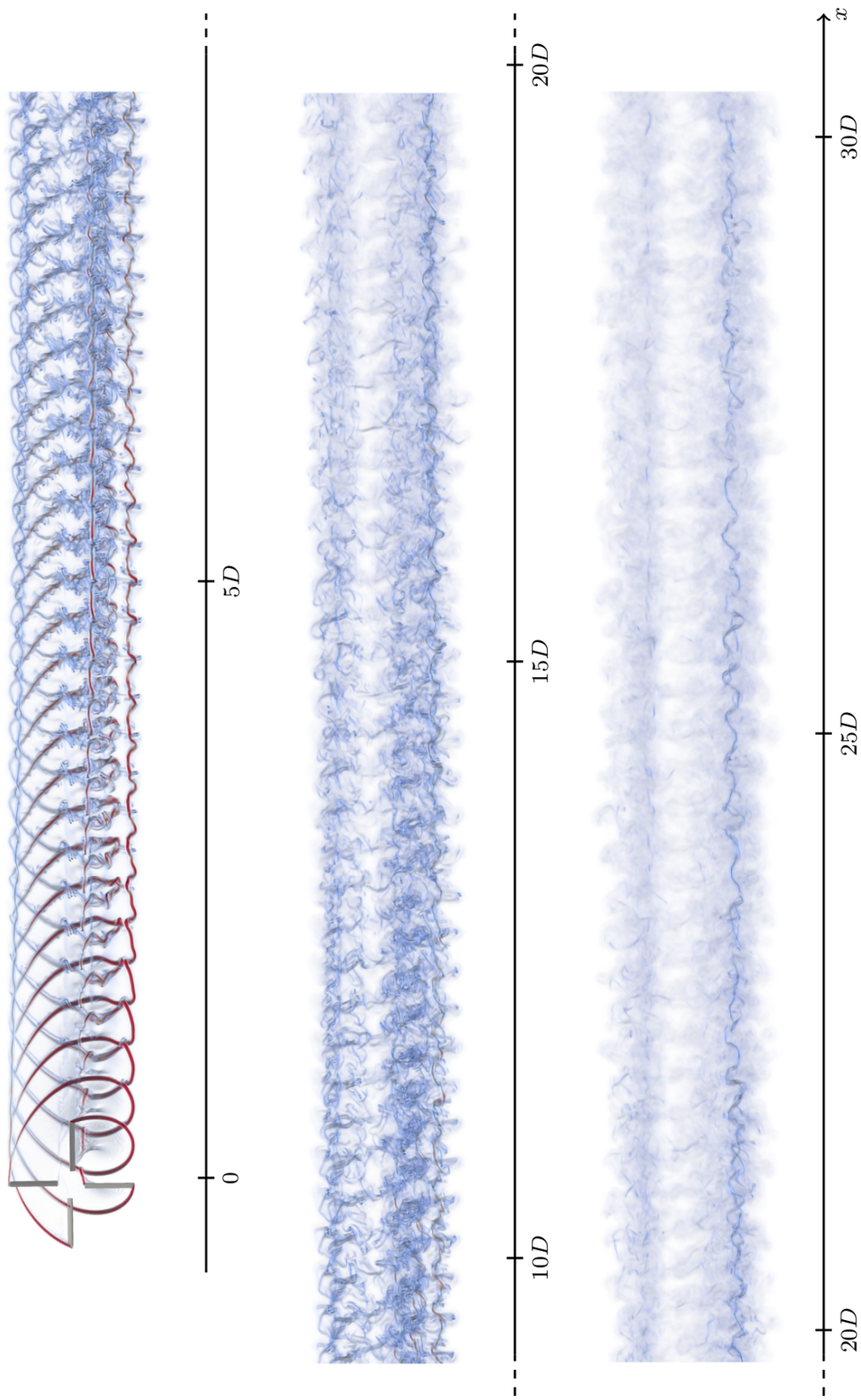


Figure 10. Top view of the near to far wake of the rotor at $\mu = 0.41$.

ACCEPTED MANUSCRIPT

where $\Gamma_0 b_0 = I$ is the linear impulse of the wake vortices. In the present wake, we measure the two-dimension (2-D) linear impulse in a cross section,

$$\Gamma_w b_w = I_w = \int_{-\infty}^{\infty}\int_{-\infty}^{\infty} y\,\bar{\omega}_x\,dy\,dz, \tag{11}$$

where $\bar{\omega}_x$ is the time-averaged axial vorticity. Then, Γ_w is the total circulation of the wake vortices and b_w is the effective spacing between the vorticity centroids.

In the wake of a wing, the shed vorticity is essentially oriented streamwise. Hence, the 2-D impulse measured in any cross section is conserved during the rollup, and $\Gamma_0 b_0 = \Gamma_w b_w$. The wake of a rotor is however far more complex, due to the 3-D shedding by the blades, and we need to closely investigate the behaviour of the 2-D impulse as a function of x.

More accurately, the force imparted by the rotor on the fluid can be recovered from a control volume analysis. Inspired by the work by Noca, Shiels, and Jeon[53], we express the time-averaged force as

$$\frac{\langle \mathbf{F}\rangle}{\rho} = \int_\Omega \langle \mathbf{u}\wedge\boldsymbol{\omega}\rangle\, dV + \frac{1}{2}\oint_{\partial\Omega} \mathbf{x}\wedge\left[\hat{\mathbf{n}}\wedge\langle \mathbf{u}\wedge\boldsymbol{\omega}\rangle\right] dS \tag{12}$$

$$= \int_\Omega \langle \mathbf{u}\wedge\boldsymbol{\omega}\rangle\, dV + \oint_{\partial\Omega} \left((P_0)_\infty - \langle P_0\rangle\right)\hat{\mathbf{n}}\, dS, \tag{13}$$

where $\langle . \rangle$ denotes the time-averaging operation (also written $\bar{.}$ hereafter), Ω is the control volume, and P_0 is the total pressure. We here neglected the contribution from the viscous and sub-grid scale stress tensors. The volume integral of $\mathbf{u}\wedge\boldsymbol{\omega}$ is referred to as the *vortex force*. Notice that, because the vorticity is a compact vector field, the integral over the boundary of Ω can be reduced to the contribution from its downstream face, S_x, i.e. a cross section of the flow. In what follows, the position x of this surface is varied.

We measure the 2-D impulse and the time-averaged force, exploiting data over a period of 10 rotor revolutions. The lift-related integrals are presented in Fig. 11, and show a good agreement with the expected C_L (Table II). The total amount of lift measured in the wake is around $C_L = 0.2327$ at $\mu = 0.25$ and $C_L = 0.0906$ at $\mu = 0.41$. The properly non-dimensionalized 2-D impulse measured in the cross section S_x is in fact very close to the lift coefficient, except in the near wake. This small deviation will be explained hereafter. Even with the complex 3-D wake that we observed, it is still remarkable that almost all the lift is signed in the 2-D impulse, already as off the early stage of the wake.

Physics of Fluids
This is the author's peer reviewed, accepted manuscript. However, the online version of record will be different from this version once it has been copyedited and typeset.
PLEASE CITE THIS ARTICLE AS DOI:10.1063/5.0015162
AIP Publishing

ACCEPTED MANUSCRIPT
Physics of Fluids
This is the author's peer reviewed, accepted manuscript. However, the online version of record will be different from this version once it has been copyedited and typeset.
PLEASE CITE THIS ARTICLE AS DOI:10.1063/5.0015162
AIP Publishing

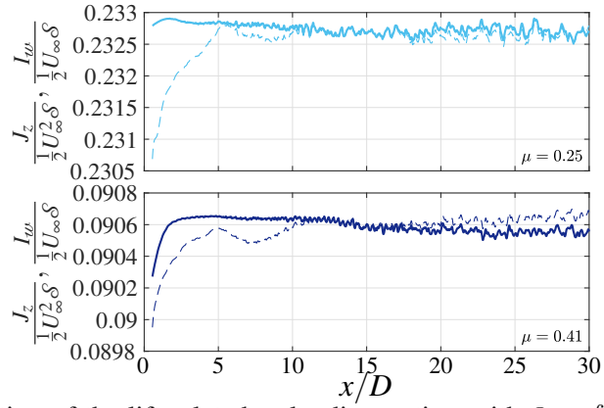


Figure 11. Spatial evolution of the lift-related wake diagnostics, with $J_z = \int_{-\infty}^{x} \int_{S_x} \langle \mathbf{u} \wedge \boldsymbol{\omega} \rangle \cdot \hat{\mathbf{e}}_z \, dS dx$ (—) and $I_w = \Gamma_w b_w$ (- -).

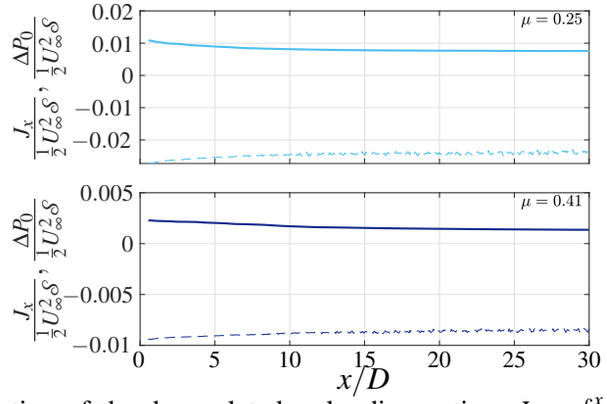


Figure 12. Spatial evolution of the drag-related wake diagnostics: $J_x = \int_{-\infty}^{x} \int_{S_x} \langle \mathbf{u} \wedge \boldsymbol{\omega} \rangle \cdot \hat{\mathbf{e}}_x \, dS dx$ (—), $\Delta P_0 = \frac{1}{2} \int_{S_x} (\mathbf{x} \wedge (\hat{\mathbf{e}}_x \wedge \langle \mathbf{u} \wedge \boldsymbol{\omega} \rangle)) \cdot \hat{\mathbf{e}}_x \, dS$ (- -).

The total amount of drag as measured in the wake (Fig. 12) is quite constant over various x stations, with $C_D = -0.0164$ at $\mu = 0.25$ and $C_D = -0.0072$ at $\mu = 0.41$. The splitting of the drag into the J_x and ΔP_0 contributions reveals a vortex force that measures some sort of induced drag (> 0). The surface integral, on the other hand, has thrust as a net result. Indeed, the forward tilting of the rotor shaft enables the production of thrust on the rotor, in this case even more for the intermediate advance ratio.

We recall that the present ILL model does not shed in the flow the additional vorticity that would, in reality, be associated with separated boundary layers and other parasitic drag effects. Nevertheless, we verify that this has only a small influence on the total drag recovered from the wake survey because the vortex dipole (i.e. the parasitic drag) signature is of opposite sign on the advancing and on the retreating side. Note that we here use the "airplane" definition of C_D which measures the force along the streamwise axis only, i.e. not accounting for the torque as conventionally done when computing the helicopter effective drag[54].

Besides, as opposed to aircraft wakes, the rotor also produces a small side force in the wake (not presented here). This force is here smaller than what would be observed on a more realistic configuration, where its largest contribution comes from the anti-torque device (vertical fin or tail rotor).

In the preliminary study[28], we also showed that, as a consequence of rotor trimming, the wake exhibits a zero rolling moment. The latter is related to the angular impulse measured in a wake cross section, $A_{\omega} = \frac{1}{3}\int_{S_x} \mathbf{x} \wedge (\mathbf{x} \wedge \bar{\boldsymbol{\omega}})\, dS$ (not shown here).

C. Statistics in slices

1. *Spanwise circulation distribution*

A useful diagnostic of the wake consists in measuring the spanwise circulation distribution:

$$\Gamma(y) = -\int_{\infty}^{y} \left(\int_{-\infty}^{\infty} \bar{\omega}_x(x, y', z')\, dz' \right) dy'. \tag{14}$$

This quantity is correlated to the vorticity production and the roll-up mechanisms on the rotor disk. Obviously, $\Gamma(y)$ is symmetrical in the wake of a wing, but this is not the case for a rotor, as seen in Figs. 13. The maximum circulation shifts toward the advancing side, indicating that vorticity spreads more laterally on the retreating side.

At a moderate advance ratio, the curve progressively relaxes towards a symmetric configuration (even more so in the far wake), under the influence of turbulent diffusion. At high advance ratio, relaxation still operates, but the distribution at $x/D = 25$ bears a noticeable asymmetry. The advancing side vortex has a more compact vortex core generated by the merging of blade tip vortices, that will be characterized in more details in Section V D. On the retreating side, interactions of vortices seem to induce a depletion of axial vorticity in the inboard part of the wake.

As an easier way to visualize it, the mean axial vorticity $\bar{\omega}_x$ is presented in Figs. 14 and 15. The forming 2-VS can be seen as early as three diameters behind the rotors, through "tip vortices". In between them, small patches of coherent, opposite sign vorticity (even from a time-averaged perspective) attest the presence of the secondary structures. Further downstream, these patches tend to smear and the main vortices tend to grow, due to the interactions between vortices of different size and strength, as discussed previously. In the far wake, the simulation at $\mu = 0.25$ has

ACCEPTED MANUSCRIPT
Physics of Fluids
This is the author's peer reviewed, accepted manuscript. However, the online version of record will be different from this version once it has been copyedited and typeset.
PLEASE CITE THIS ARTICLE AS DOI:10.1063/5.0015162
AIP Publishing

ACCEPTED MANUSCRIPT
Physics of Fluids
This is the author's peer reviewed, accepted manuscript. However, the online version of record will be different from this version once it has been copyedited and typeset.
PLEASE CITE THIS ARTICLE AS DOI:10.1063/5.0015162
AIP Publishing

produced two essentially homogeneous vortices (in the mean), thus close to a fully rolled-up state. At $\mu = 0.41$ however, large turbulent patches of same-sign vorticity are still observable outside of the main vortices, indicating that the roll-up is not fully completed.

We also notice that, at high advance ratio, the vortex core originating from the advancing side appears to travel downwards at a higher pace than that of the retreating side. This, however, must not be interpreted as an imbalance in the rotor wake: the vorticity centroids, also shown on the slices, indeed descend at the same velocity.

2. *Wake circulation and spacing*

We examine the measured circulation of one wake vortex, Γ_w. Given the wake asymmetry, the center of the wake y_c satisfies

$$\int_{-\infty}^{y_c} \Gamma(y)\, dy = \int_{y_c}^{\infty} \Gamma(y)\, dy. \tag{15}$$

This y_c also corresponds to the spanwise coordinate of the point of application of the lift force. Then, the wake vortex circulation is obtained as $\Gamma_w = \Gamma(y_c)$ (with the starboard vortex circulation Γ_w and the port vortex circulation $-\Gamma_w$) and the effective spacing as $b_w = I_w/\Gamma_w$. Note that, in the present cases, and despite the asymmetry in the spanwise circulation distribution, the wake center location remains close to $y_c = 0$. Indeed, it must be so as we have ensured that the rotor is trimmed in roll. (If it was not the case, the point of application of the lift would be shifted in y.) This further confirms that there is no angular momentum in the wake, and that the wake mid-plane can be assumed to be vertical at every location z.

The vortex circulation and effective spacing measured in the simulations are shown in Figs. 16

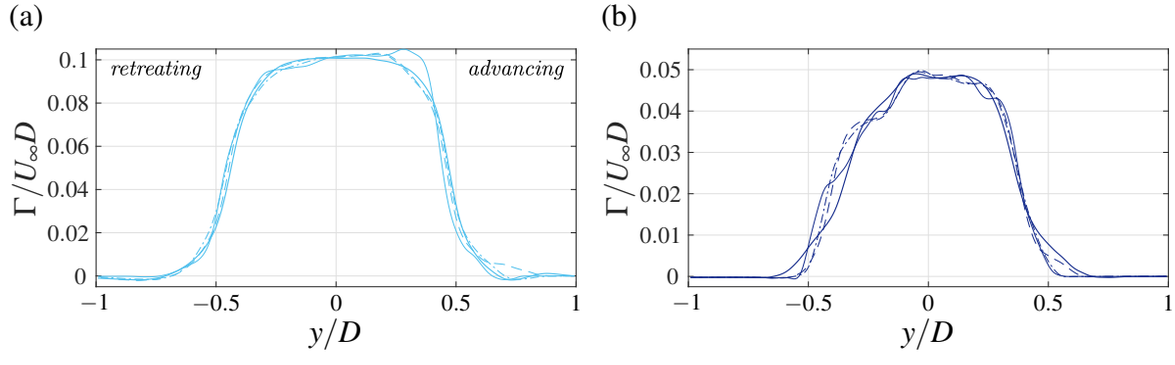


Figure 13. Time-averaged spanwise circulation distribution of the wake, for (a) $\mu = 0.25$ and (b) $\mu = 0.41$, at $\frac{x}{b} = 10$ (—), 15 (- -), 20 (- -) and 25 (—).

ACCEPTED MANUSCRIPT
Physics of Fluids
This is the author's peer reviewed, accepted manuscript. However, the online version of record will be different from this version once it has been copyedited and typeset.
PLEASE CITE THIS ARTICLE AS DOI:10.1063/5.0015162
AIP Publishing

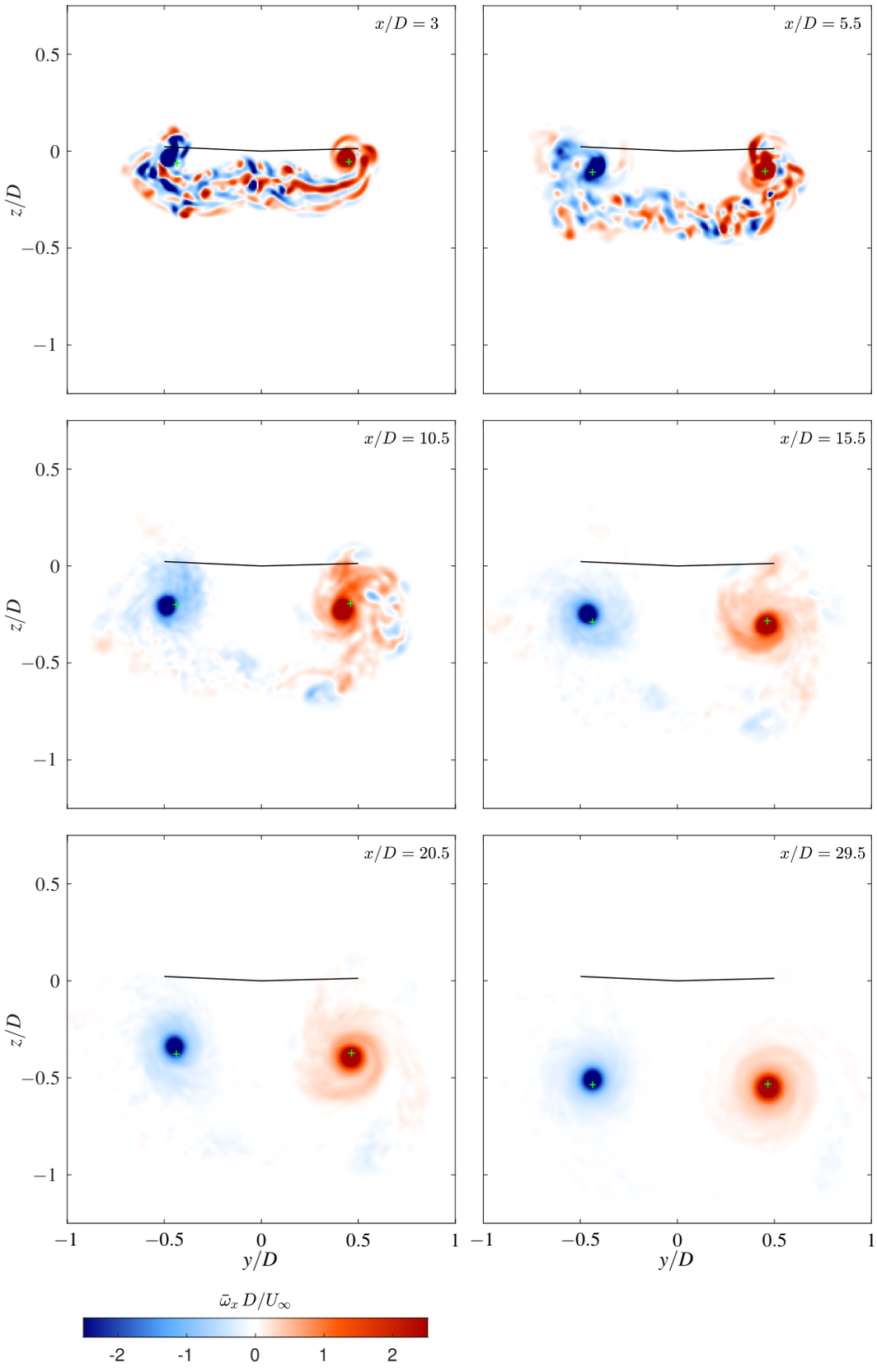


Figure 14. Mean streamwise vorticity ($\bar{\omega}_x$) for $\mu = 0.25$. Vorticity centroids (+).

ACCEPTED MANUSCRIPT
Physics of Fluids
This is the author's peer reviewed, accepted manuscript. However, the online version of record will be different from this version once it has been copyedited and typeset.
PLEASE CITE THIS ARTICLE AS DOI:10.1063/5.0015162
AIP Publishing

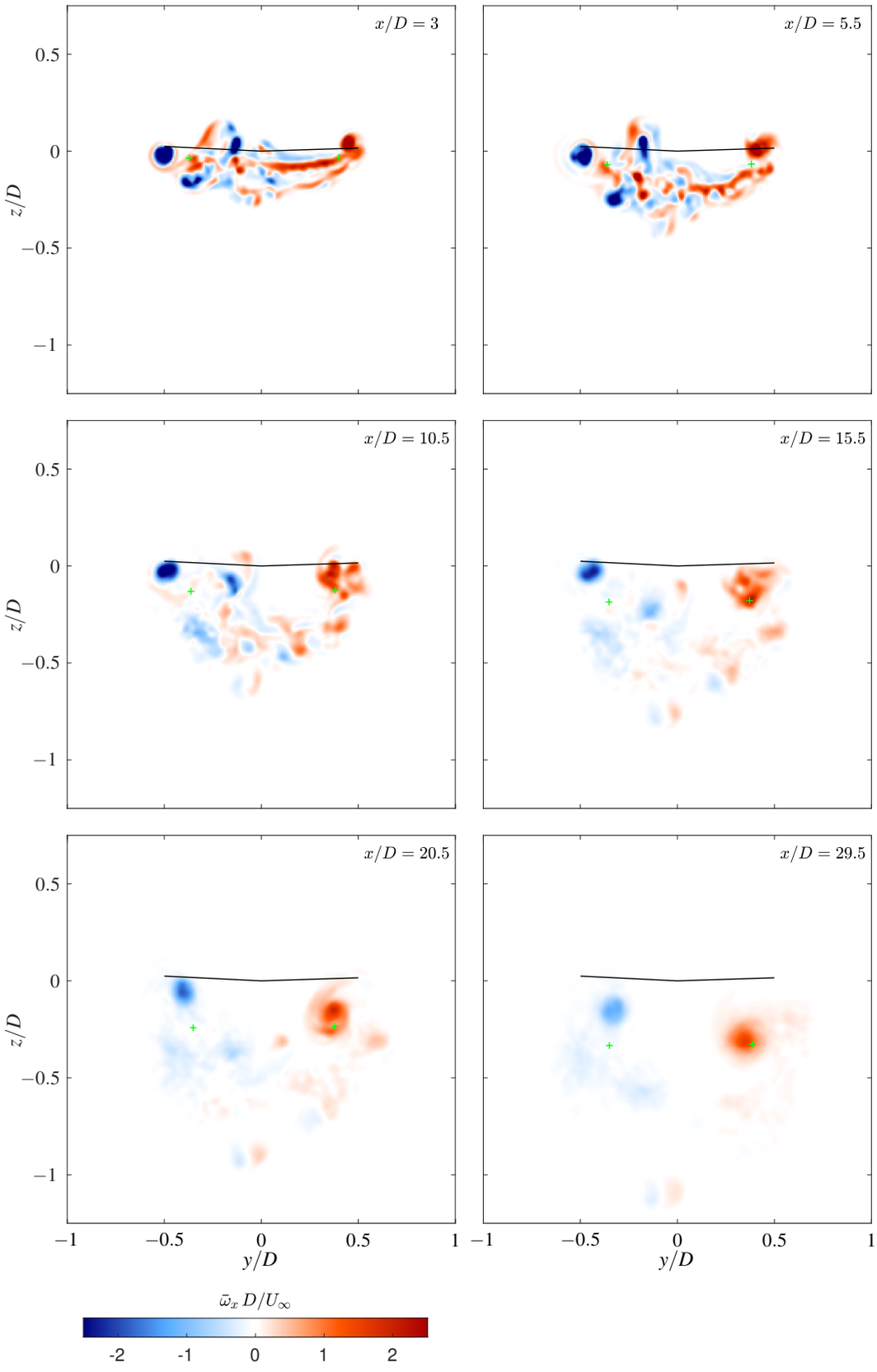


Figure 15. Mean streamwise vorticity ($\bar{\omega}_x$) for $\mu = 0.41$. Vorticity centroids (+).

ACCEPTED MANUSCRIPT
Physics of Fluids
This is the author's peer reviewed, accepted manuscript. However, the online version of record will be different from this version once it has been copyedited and typeset.
PLEASE CITE THIS ARTICLE AS DOI:10.1063/5.0015162
AIP Publishing

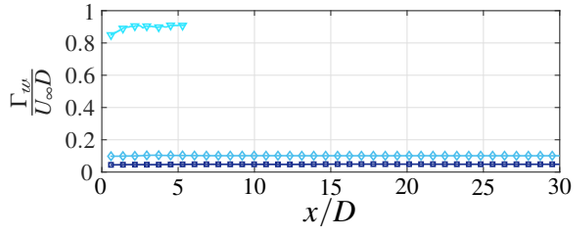


Figure 16. Streamwise evolution of the wake circulation, for $\mu = 0.08$ ( ), $\mu = 0.25$ ( ) and $\mu = 0.41$ ( ).

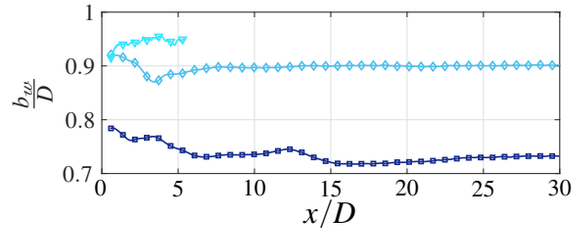


Figure 17. Streamwise evolution of the vortex separation, for $\mu = 0.08$ ( ), $\mu = 0.25$ ( ) and $\mu = 0.41$ ( ).

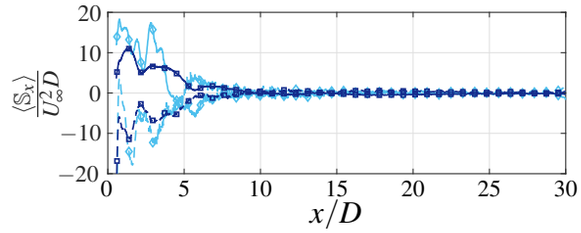


Figure 18. Streamwise evolution of the axial stretching integrated over the half plane $\mathbb{S}_x = \int_{S_x^{+/-}} (\boldsymbol{\omega} \cdot \nabla \mathbf{u}) \cdot \hat{\mathbf{e}}_x d\mathbf{x}$, for $\mu = 0.25$ ( ) and $\mu = 0.41$ ( ). Half plane left (S_x^-, dashed) and half plane right (S_x^+, solid).

and 17. The smaller the advance ratio, the faster the establishment of a constant Γ_w and b_w. The final spacing is shorter for high advance ratios, whereas it reaches almost $0.95D$ at $\mu = 0.08$. Initially, a small variation of Γ_w (within $\sim 5\%$) can also be seen in all cases.

During the wake roll-up, there is a global process of transition from a complex wake dominated by 3-D tip vortices to a 2-D wake overwhelmed by two main streamwise vortices. In the near wake, transverse vorticity (ω_y, ω_z) originates in the shedding from the blades which occurs continuously over one revolution. The associated transverse vorticity structures, which are specific to rotorcraft applications, must then realign in the streamwise direction. We show that the vortex stretching is responsible for this alignment, intensified during the many vortex-vortex interactions previously described. A measure of this phenomenon is provided by the stretching term of the Navier-Stokes

ACCEPTED MANUSCRIPT
Physics of Fluids
This is the author's peer reviewed, accepted manuscript. However, the online version of record will be different from this version once it has been copyedited and typeset.
PLEASE CITE THIS ARTICLE AS DOI:10.1063/5.0015162
AIP Publishing

equations, $\mathbb{S}$, which we integrate over each half of the cross section of the flow, respectively S_x^- and S_x^+ for the retreating and the advancing sides (Fig. 18). In the near wake, its streamwise component is negative on the retreating side and positive on the advancing side. As a result, negative and positive streamwise vorticity components are respectively injected in the 2-VS, thus increasing Γ_w. Besides, the intensity of the stretching rapidly decreases behind the rotor and it almost reaches zero at $x = 10D$ for all advance ratios. This is consistent with the establishment of a constant I_w. The canceling of the stretching activity indicates the end of the transverse vorticity alignment process. However, it does not mean the end of the roll-up itself: it takes more time for the now essentially axial vorticity to concentrate and to form main coherent vortices, as can be observed at $x/D = 29.5$ in the high advance ratio case.

3. *Energies*

This spatial evolution of the energies in the 2-VS is shown in Fig. 19. The roll-up is characterized by a steeper descent in the total energy per slice, comparatively to what is observed in the wake of wings[55]. After roll-up, the decrease is much slower, but still surpasses that observed in the wake of wings. The turbulent kinetic energy (TKE), i.e. the energy of the fluctuations, contributes significantly to the total energy, especially in the near wake and for the high advance ratio.

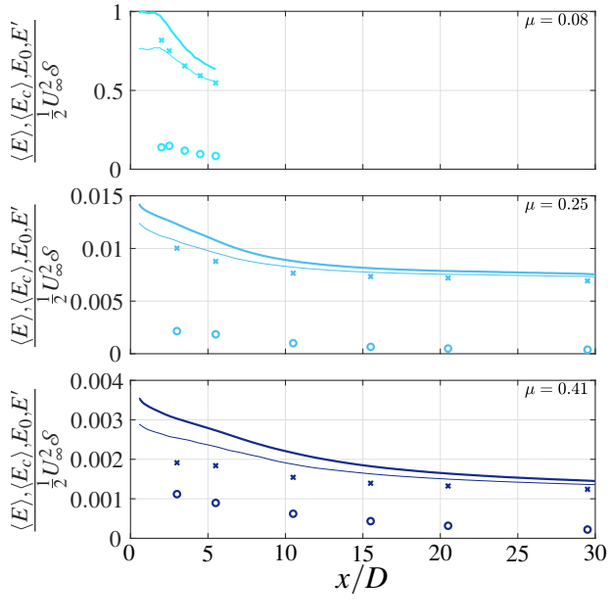


Figure 19. Spatial evolution of energies integrated in a cross section: $\langle E\rangle = \frac{1}{2}\int_{S_x} \langle (\mathbf{u}-\mathbf{U}_\infty)\cdot(\mathbf{u}-\mathbf{U}_\infty)\rangle \, dS$ (—), $\langle E_c\rangle = \frac{1}{2}\int_{S_x} \langle u_y^2 + u_z^2\rangle \, dS$ (—), $E_0 = \frac{1}{2}\int_{S_x} \left((\bar{u}_x - U_\infty)^2 + \bar{u}_y^2 + \bar{u}_z^2\right) dS$ (×), and $E' = \int_{S_x} \mathrm{TKE}\, dS$ (○).

ACCEPTED MANUSCRIPT
Physics of Fluids
This is the author's peer reviewed, accepted manuscript. However, the online version of record will be different from this version once it has been copyedited and typeset.
PLEASE CITE THIS ARTICLE AS DOI:10.1063/5.0015162
AIP Publishing

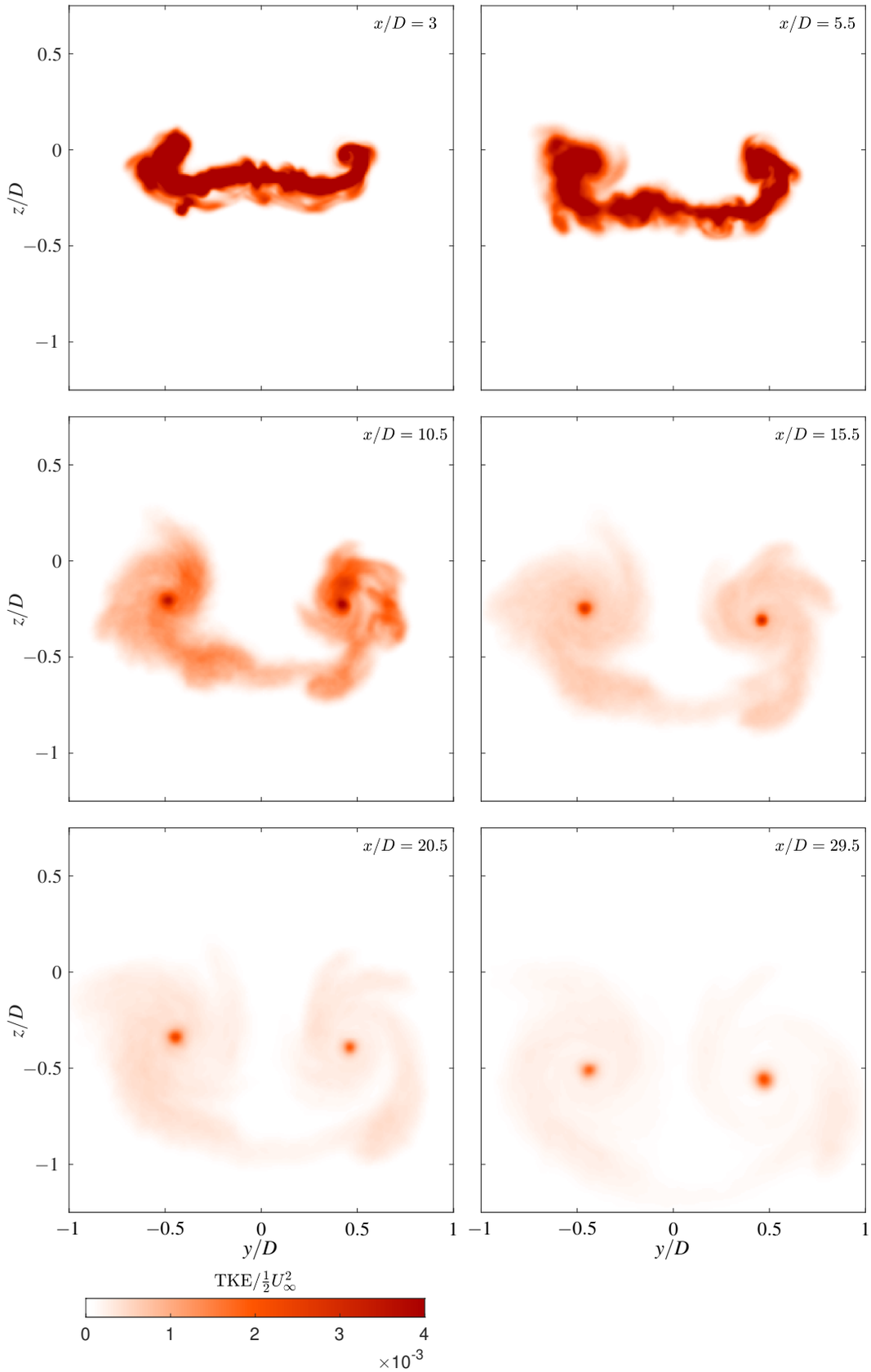


Figure 20. Turbulent kinetic energy at $\frac{x}{D} = 2.5, 5, 10, 15, 20, 25$ for $\mu = 0.25$.

ACCEPTED MANUSCRIPT
Physics of Fluids
This is the author's peer reviewed, accepted manuscript. However, the online version of record will be different from this version once it has been copyedited and typeset.
PLEASE CITE THIS ARTICLE AS DOI:10.1063/5.0015162
AIP Publishing

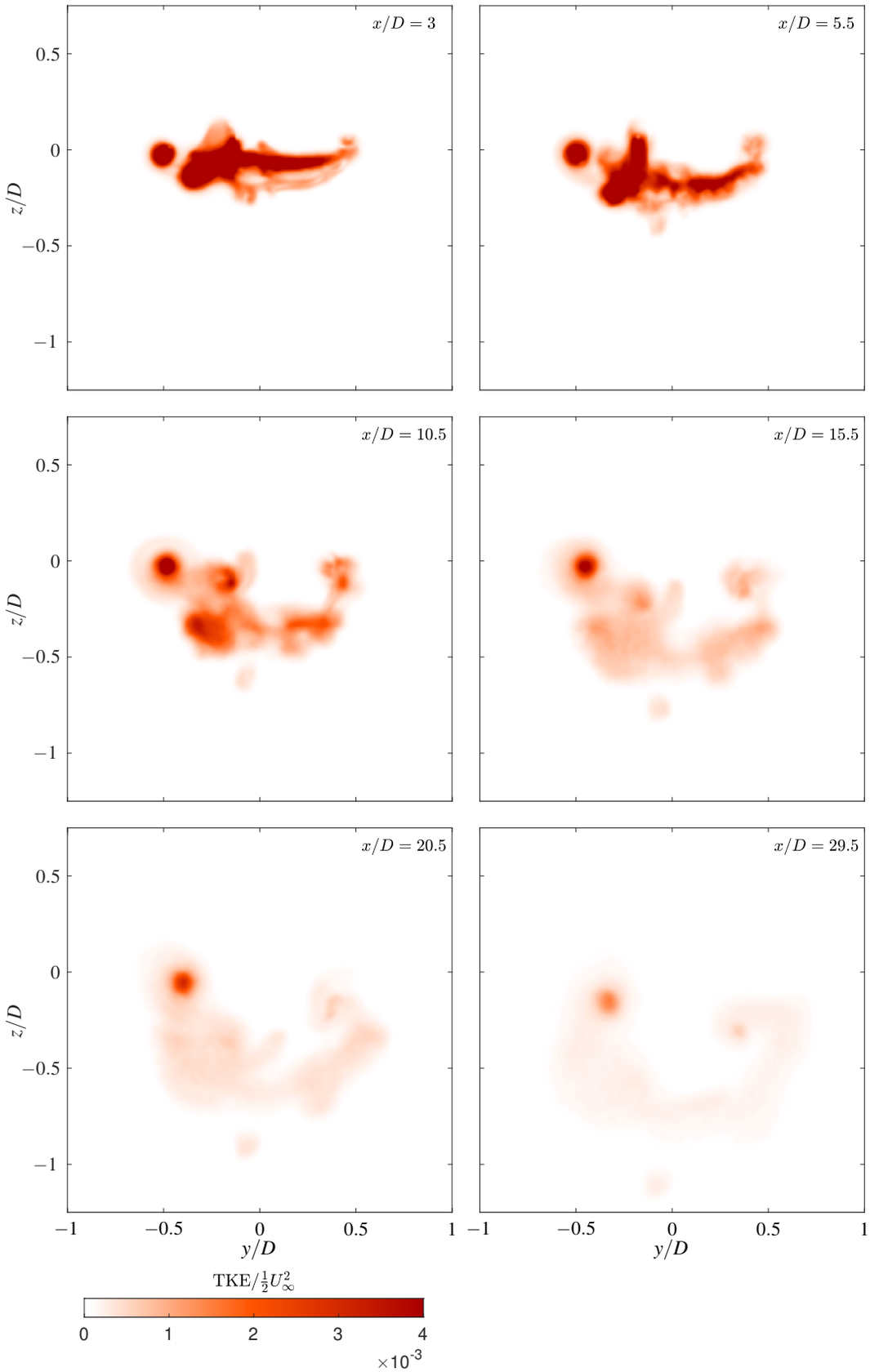


Figure 21. Turbulent kinetic energy at $\frac{x}{D} = 2.5, 5, 10, 15, 20, 25$ for $\mu = 0.41$.

The spatial distribution of TKE is monitored across the slices, Fig. 20 and Fig. 21. Areas where the TKE is significant (and is thence also dissipated) are mainly located:

- Close to the center of the main wake vortices. It can be explained by the blade tip vortices merging and reconnections (resp. on the advancing and retreating side) generating turbulence which is progressively diffused;

- In the area downstream of the reverse flow region, with a greater effect at high advance ratio. As already noticed, the intense shedding occurring in that zone triggers strong interactions with the surrounding (more coherent) vortices, with the fast increase in turbulence as a result. This process contributes to the homogenization of the mean flow.

Clearly, the missing elements in the simulation (with respect to an actual rotorcraft, i.e. the fuselage, the hub, the tail rotor, etc.) would result in an even broader high TKE zone in the wake.

In order to further quantify the transition from a 3-D flow in the near wake to an almost 2-D flow in the far wake, we consider the ratio between the 3-D kinetic energy and the energy of the cross flow (Fig. 22). At low advance ratio, the streamwise component of velocity accounts for a significant portion of the total energy in the near wake. However, the transition to the 2-VS also occurs on a shorter distance: the lower the μ, the steeper the gradient of $\frac{\langle E \rangle}{\langle E_c \rangle}$. Indeed, as the successive tip vortices are closer to each other at a low advance ratio, the near wake system is prone to the faster development of vortex interactions.

4. Axial scaling of the roll-up

It has become clear, from the qualitative description of the wake and from the above spatial diagnostics, that the physical distance over which the roll-up occurs depends on the advance ratio. However, we may try to determine a re-scaling of the data along the streamwise axis such that the description of the roll-up becomes independent of the advance ratio. To this purpose, we consider the use of time instead of space. We propose to describe the age of the vortex system using the same convention as for aircraft vortices, and we hence define the reference time unit as the time required for the rolled-up vortices to descend one vortex spacing, $t_0 = \frac{b_0}{V_0}$, where $V_0 = \frac{\Gamma_0}{2\pi b_0}$ is the nominal descent velocity of the vortices. We here estimate Γ_0 (resp. b_0) using the value of Γ_w (resp. b_w) in the far wake (i.e. towards the end of the roll-up), where they are fairly constant. The

ACCEPTED MANUSCRIPT
Physics of Fluids
This is the author's peer reviewed, accepted manuscript. However, the online version of record will be different from this version once it has been copyedited and typeset.
PLEASE CITE THIS ARTICLE AS DOI:10.1063/5.0015162
AIP Publishing

ACCEPTED MANUSCRIPT
Physics of Fluids
This is the author's peer reviewed, accepted manuscript. However, the online version of record will be different from this version once it has been copyedited and typeset.
PLEASE CITE THIS ARTICLE AS DOI:10.1063/5.0015162
AIP Publishing

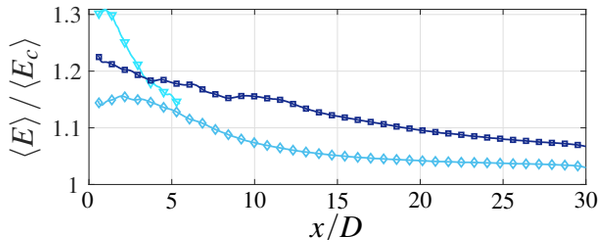


Figure 22. Streamwise evolution of the ratio between the 3-D energy and the energy of the cross flow, for $\mu = 0.08$ (▽), $\mu = 0.25$ (◇) and $\mu = 0.41$ (▭).

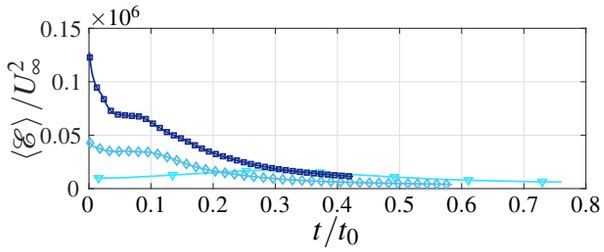


Figure 23. Streamwise evolution of the enstrophy, for $\mu = 0.08$ (▽), $\mu = 0.25$ (◇) and $\mu = 0.41$ (▭).

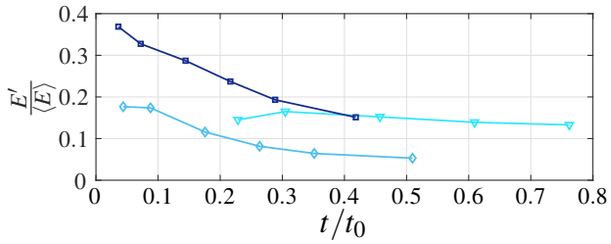


Figure 24. Streamwise evolution of the ratio between the energy of the fluctuations and the total kinetic energy, for $\mu = 0.08$ (▽), $\mu = 0.25$ (◇) and $\mu = 0.41$ (▭).

spatial coordinate is thus transformed following

$$\frac{t}{t_0} = \frac{(x-R)}{U_\infty}\frac{V_0}{D}\frac{D}{b_0} \simeq \frac{(x-R)}{D}\phi\frac{D}{b_0}, \tag{16}$$

where the slope of the wake simplifies to $\phi = \frac{1}{4}\left(\frac{D}{b_0}\right)^2 C_L \simeq \frac{1}{4}\left(\frac{D}{b_0}\right)^2 \mu^2 C_T$ for the case of rotors.

When properly rescaled, the enstrophy, $\mathscr{E} = \int_{S_x} \langle \boldsymbol{\omega} \cdot \boldsymbol{\omega} \rangle \, dS$ (Fig. 23), exhibits a very similar behavior for all advance ratios. This supports the idea that, after the alignment of the transverse vorticity, the wake decay can indeed be characterized independently of the rotor advance ratio. Logically, it seems however not possible to determine universally the end of this alignment process, independently of the advance ratio.

ACCEPTED MANUSCRIPT
Physics of Fluids
This is the author's peer reviewed, accepted manuscript. However, the online version of record will be different from this version once it has been copyedited and typeset.
PLEASE CITE THIS ARTICLE AS DOI:10.1063/5.0015162
AIP Publishing

The ratio between the energy of the fluctuations E' and the total kinetic energy $\langle E \rangle$, Fig. 24, appears to reach a plateau within the simulations at low and moderate advance ratios. This might corroborate the existence of a turbulent 2-VS at statistical equilibrium. Such a state, which was observed in past numerical studies[56,57], is reached when the fully formed vortex system smoothly decays while sustaining its own turbulence.

A well-developed 2-VS was thus reached within the computational domain at the low and medium advance ratios; but not yet a the high advance ratio. While it is commonly assumed that the roll-up of aircraft wakes is completed as early as 10 to 15 wingspans downstream of the wing, such a criterion (based on the rotor diameter) clearly cannot exist for rotorcraft, because of the influence of the advance ratio on the vortex dynamics. Using the vortex reference time unit instead, we postulate that the roll-up may take as long as $t_0/2$ to t_0. This time is required for the axial vorticity to concentrate so as to form essentially axisymmetric vortices. For larger t/t_0, the wake circulation (which was here fairly constant in the simulated far wake, Fig. 16) should also start decreasing by the turbulent exchange of vorticity through the wake mid-plane, thus leading to a slow decay of Γ_w. This is observed in aircraft wakes as well[55].

In their evolution towards an axisymmetric state, we now examine the radial distributions of circulation and azimuthal velocity, which characterize the vortices at different locations in the wake.

D. Velocity and circulation distributions in the wake vortices

We aim to obtain the circulation distribution of the vortices and to compare it qualitatively with typical wing results. However, while the vortex cores remain coherent all along the roll-up process in aircraft applications, the instantaneous flow field in a cross-section behind the rotor is much more chaotic. In particular, the identification of the vortex center from the maximum of vorticity is sometimes impossible on the instantaneous vorticity field. Hence, we compute the circulation distribution of the time-averaged vortex,

$$\Gamma(x,r) = \int_0^r \int_0^{2\pi} \bar{\omega}(x,r',\theta)\, r'\, d\theta\, dr'. \tag{17}$$

ACCEPTED MANUSCRIPT
Physics of Fluids
This is the author's peer reviewed, accepted manuscript. However, the online version of record will be different from this version once it has been copyedited and typeset.
PLEASE CITE THIS ARTICLE AS DOI:10.1063/5.0015162
AIP Publishing

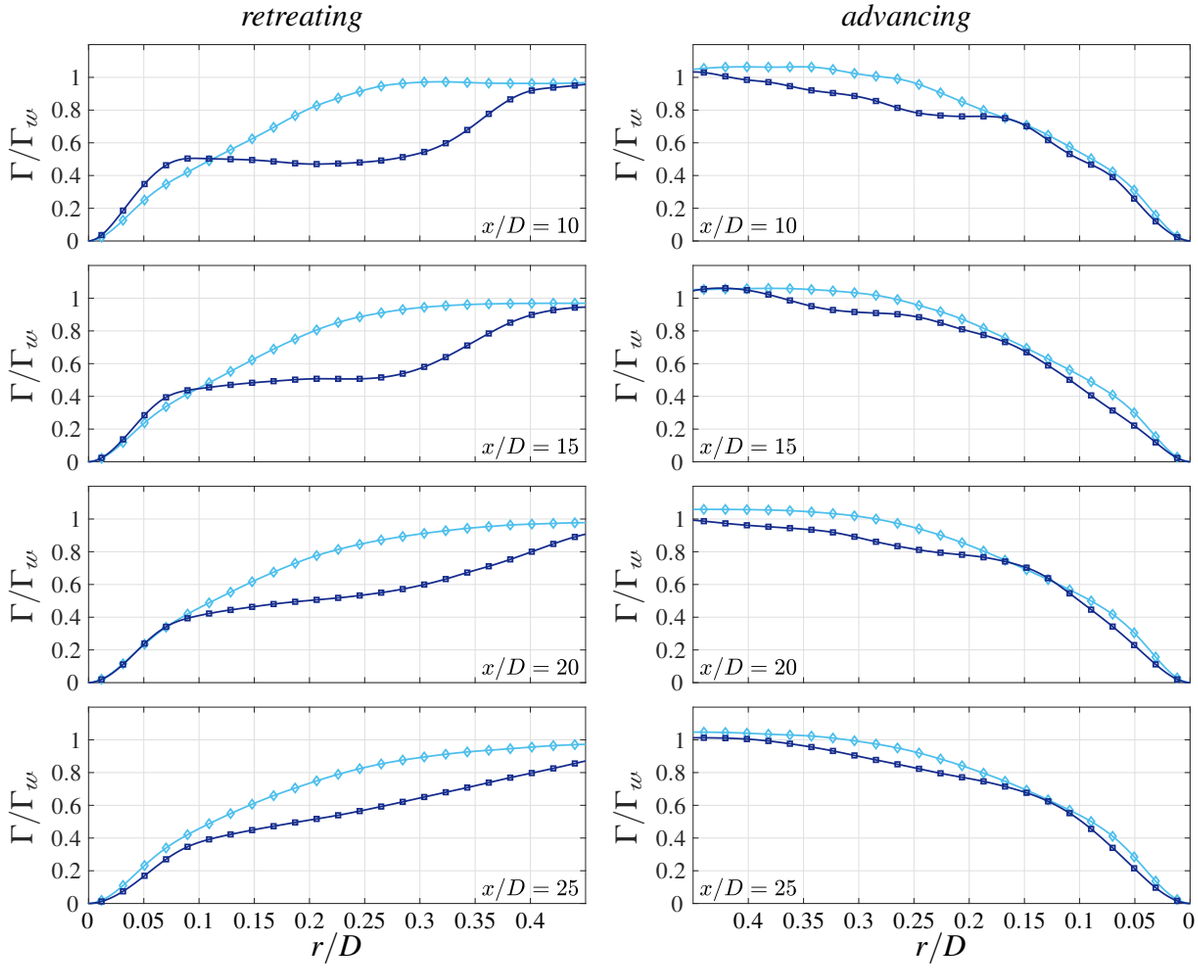


Figure 25. Circulation distribution of each mean vortex for $\mu = 0.25$ (◇) and $\mu = 0.41$ (□).

Similarly, we define the azimuthal velocity induced by one mean vortex,

$$\bar{u}_\theta(x,r) = \frac{\Gamma(x,r)}{2\pi r}. \tag{18}$$

The corresponding effective core radius of the mean vortex, $r_c(x)$, is then defined as the radius at which this velocity is maximum.

The circulation distribution and induced azimuthal velocity of the mean vortices are presented respectively in Figs. 25 and 26. The advancing side and the retreating side vortices are quite dissimilar, even more at high advance ratio. Once again, we observe the larger spreading of the vorticity on the retreating side. Both vortices progressively relax toward a smooth circulation distribution, however with a mean vortex much less compact than what is reported from the study of the aircraft wakes[58]. Indeed, the r_c/D is of the order of 10% for both advance ratios (and

ACCEPTED MANUSCRIPT
Physics of Fluids
This is the author's peer reviewed, accepted manuscript. However, the online version of record will be different from this version once it has been copyedited and typeset.
PLEASE CITE THIS ARTICLE AS DOI:10.1063/5.0015162
AIP Publishing

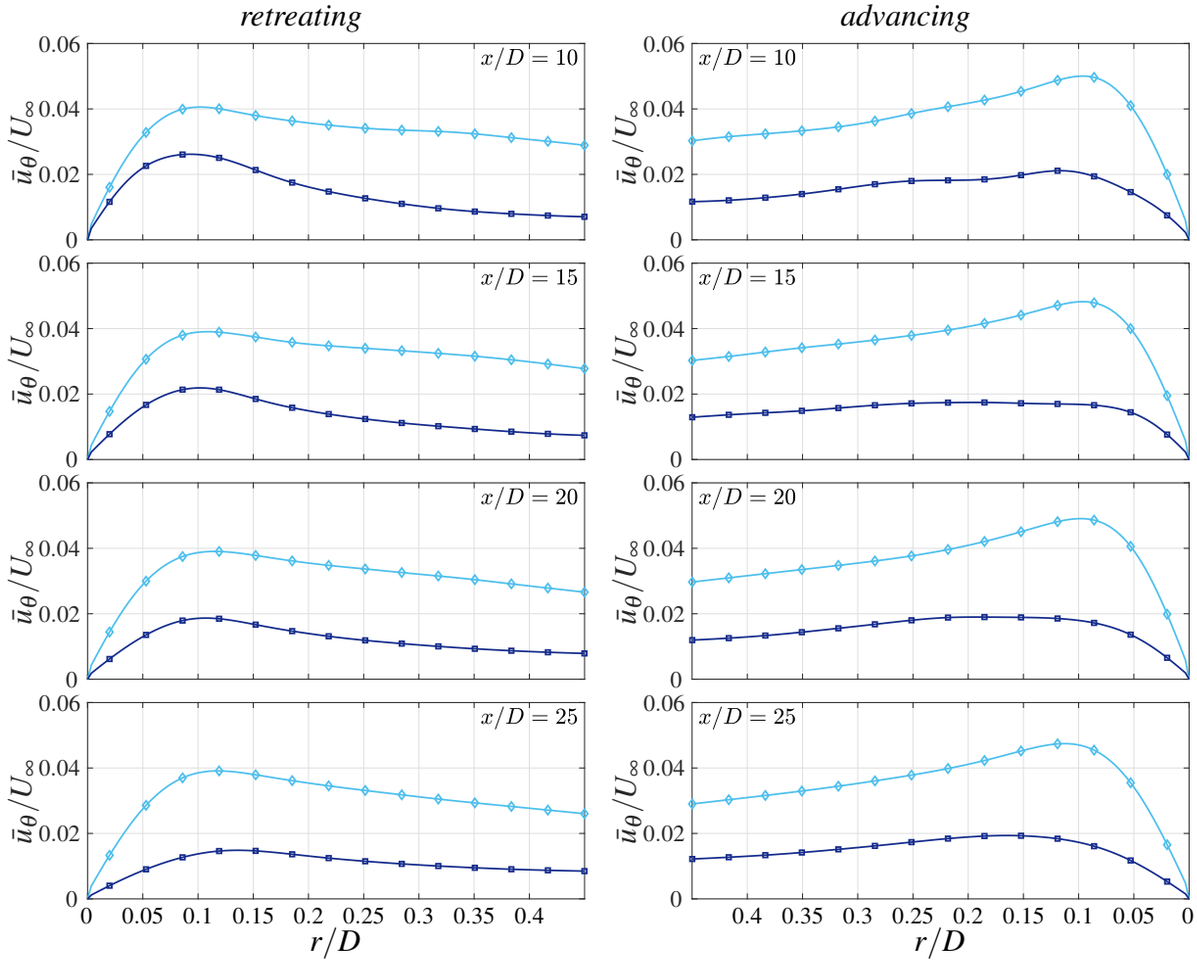


Figure 26. Azimuthal velocity induced by each mean vortex for $\mu = 0.25$ (◇) and $\mu = 0.41$ (▭).

still grows in the far wake). This is twice as much as typical aircraft wing mean vortex radii. This results from the complex roll-up process and the underlying vortex dynamics, through the merging of tip vortices and the subsequent transverse vorticity alignment. Inherent to this unsteady wake generation process, periodic fluctuations may still persist in the far wake, and are discussed in the next section.

E. Time periodicity in the wake and disappearance of rotor harmonics

Finally, we study the evolution of the time periodicity in the wake of the rotor. Close to the rotor, the flow is overwhelmed by the tip vortices, hence the main flow features will occur at the blade passage frequency (BPF). With the subsequent interaction of these features (including vortex reconnections, vortex mergers, and the associated generation of smaller-scale structures),

we expect to observe a loss of periodicity in the far wake. We here study the progression of this process over space (in the streamwise direction) by identifying the signature of the BPF and of harmonics on the kinetic energy, and by quantifying their strength.

At a given location x, we consider the kinetic energy of the perturbation flow, integrated in a cross section, $E(t,x) = \frac{1}{2}\int_{S_x}(\mathbf{u}-\mathbf{U}_\infty)\cdot(\mathbf{u}-\mathbf{U}_\infty)\,dS$. Such an integral provides a global quantity over the cross-section, i.e. it does not depend upon the choice of an arbitrary y,z location. The resulting energy is treated as a signal which still depends on space (only in the streamwise direction) and time: it is an output of our simulations. Then, as a post-processing operation, we compute the power spectral density (PSD) of $E(t,x)$ along time and for every discreet location x of our computational mesh, using fast Fourier transforms. The result is $\hat{E}(f,x)$. As we are mainly interested in the power content associated with the rotor frequencies, we only consider the "modes" corresponding to specific frequencies f. In particular, we examine the frequencies of *1* and 2 per rotor revolution (1rev, 2rev), and *1* to *4 per blade passage* (1p, 2p, 4p). For the present four-bladed rotor, we thus have that the BPF (*1p*) is equivalent to *4 per revolution*. We also report the *total power of the energy fluctuations* in the cross section, which is the sum of the PSD for all modes except the mode $f = 0$.

The spatial evolution of all these modes along the streamwise axis is presented in Fig. 27. In the very near wake, the PSD of the energy contained in the BPF mode dominates for both advance ratios, and amounts to respectively 5% and 11% of $\hat{E}(0,0)$.

At $\mu = 0.25$ (Fig. 27(a)), this quantity decreases by two orders of magnitude over 15 rotor diameters, yet in a non-monotonic way. In particular, two "sinks" are observed around $\frac{x}{D} \simeq 7$ and 11, where the PSD of the BPF mode abruptly drops by one order of magnitude, and then quickly recovers. This type of sink is also observed on higher harmonics of the BPF at different spatial locations. We postulate that they reflect vortex dynamics events associated with a specific topological feature (e.g. a stationary vortex merger or reconnection point), which are locally occulting rotor harmonics. Besides, the total power of the energy fluctuations also loses 1.5 order of magnitude by $x/D \simeq 20$, however with a smoother progression. It then re-increases to reach a pseudo-plateau beyond $x/D \simeq 25$, potentially indicative of some statistical turbulent equilibrium attained in the developed 2-VS. On the other hand, we observe that the modes associated with the subharmonics of the BPF become more significant in the distance. They even surpass the BPF mode, downsteam of $\frac{x}{D} \simeq 15$. The relative increase of these lower frequencies is consistent with the occurence of pairing and merging phenomena, as they are known to cause backscattering

ACCEPTED MANUSCRIPT
Physics of Fluids
This is the author's peer reviewed, accepted manuscript. However, the online version of record will be different from this version once it has been copyedited and typeset.
PLEASE CITE THIS ARTICLE AS DOI:10.1063/5.0015162
AIP Publishing

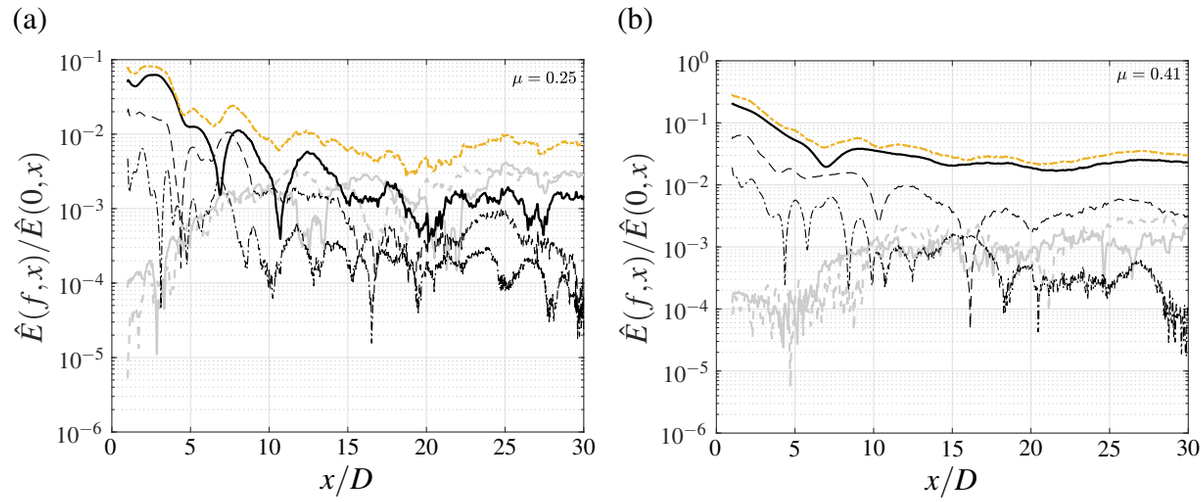


Figure 27. Spatial evolution of the power spectral density of the total kinetic energy measured in slices, restricted to the content of harmonics and sub-harmonics of the BPF, divided by the content of the mode 0: 1rev (—), 2rev (- -), 1p (—), 2p (- -), 4p (- ·-), and the sum of the PSD of all modes except mode 0 (- ·-).

of energy (small scales combining to form larger coherent scales, as also observed in wind turbine wakes). In the far wake, the PSD of the BPF mode is worth roughly 10% of the sum of all fluctuation modes whereas the higher harmonics contribute to below 1%.

Generally, similar features are observed at the higher advance ratio (Fig. 27(b)). However, the content of the BPF mode remains more prominent. It is approximately one order of magnitude larger than the energy of all other characteristic modes in the far wake, including the subharmonics. It also still accounts for roughly half of the energy of the fluctuations. Sudden drops are also observed, yet of smaller amplitude (at least on the BPF mode). This hints at differences in the dynamics of the roll-up process, with potentially weaker interactions.

Consistently with our observations of the previous sections, we have here again obtained quantitative evidence that the roll-up significantly reduces the periodic signature of the rotor in the far wake. Yet, the resulting vortex systems still bear significant traces of the periodicity inherent to the wake generation process. These traces are even more persistent in the wake of the rotor at high advance ratio, for which we already noticed that the roll-up process was not fully completed.

In all cases, our results reveal that the roll-up of the wake behind a rotor happens in two phases:

- In the initial phase, strong interactions develop between the successive tip vortices shed in the wake, the vorticity in the vortex sheets and that from the near hub region (here due to dynamic stall). These interactions are responsible for a fast loss of periodicity in the wake structures, and enable the emergence of the 2-VS. The transverse vorticity alignment

ACCEPTED MANUSCRIPT
Physics of Fluids
This is the author's peer reviewed, accepted manuscript. However, the online version of record will be different from this version once it has been copyedited and typeset.
PLEASE CITE THIS ARTICLE AS DOI:10.1063/5.0015162
AIP Publishing

process occurs during this phase, which is also characterized by a relatively fast decrease in the total kinetic energy (see Fig. 19). Moreover, the contribution of the fluctuations in the total kinetic energy rapidly decreases.

- The second phase starts when the two wake vortices are formed (at least in a time-average sense), and are surrounded by smaller intensity turbulent vortex patches ensuing from the first phase. These slowly aggregate in the main wake vortices, and the flow evolves towards a fully-developed 2-VS with essentially axisymmetric vortices, the energy of which slowly decays due to the self-induced turbulence.

VI. CONCLUSIONS

In this article, we studied the large scale aerodynamics of helicopter rotors and their wakes. Considering advancing flight, we verified the validity of our numerical method against a reference experiment of a four-bladed rotor. A comparison between the presently computed trim parameters (cyclic and collective control inputs) versus those measured experimentally showed a reasonable agreement. Then, we performed the LES of the wake of the rotor at three advance ratios ($\mu = 0.08$, 0.25 and 0.41), all the way to 30 diameters downstream. These simulations led to several insights into the vortex dynamics at play in the wake. In the near rotor region, the complex wake formation and roll-up processes (at least far more complex than those observed for fixed wings) were described. The origin of the ensuing turbulence was identified. The interactions of tip vortices of different strength and orientation is indeed propitious to pairing, merger and reconnections; all leading to the onset of turbulent conditions. Vortex shedding from the dynamic stall occurring on the inboard part of the retreating blade also contributes, but it is only significant at high advance ratios. Besides, through the analysis of 3-D visualizations, the vortex dynamics involved in the generation of the two main wake vortices was qualitatively described: merging of blade tip vortices occurring on the advancing side, and reconnections on the retreating side.

From statistics gathered in transverse slices in the near and far wake regions, the emergence and the evolution of the two-vortex system was thoroughly quantified. Compared to the wake shed by a clean aircraft wing, it must be highlighted that:

- The near wake, with all the 3-D complexity associated with the interlaced tip vortices, transitions to a mainly 2-D vortex system over a distance that depends on the advance ratio.

ACCEPTED MANUSCRIPT
Physics of Fluids
This is the author's peer reviewed, accepted manuscript. However, the online version of record will be different from this version once it has been copyedited and typeset.
PLEASE CITE THIS ARTICLE AS DOI:10.1063/5.0015162
AIP Publishing

Even though the signature in lift is prominent as early as in the near wake, we showed the existence of a process of vorticity alignment in the streamwise direction, which is connected to a net significant contribution from vortex stretching;

- The wake of the rotor is initially not symmetric, even when the rotor is trimmed, but it tends to become so in the far field;

- The circulation and azimuthal velocity distributions of the mean vortices in the 2-VS expose less compact vortices, with a much spread effective core size;

- The kinetic energy here decays much faster than in the wake of a wing. However, its evolution in the far field hints at the establishment of a turbulent equilibrium in the 2-VS, with a constant ratio between the energy of the fluctuations and the total energy.

Besides, we proposed a rescaling of the wake in the streamwise directions that enables its description in a manner less dependent on the advance ratio.

Finally, we investigated the spatial evolution of the energy stored in the rotor characteristic frequencies and harmonics. While it dominates the near wake, the blade passage frequency rapidly loses importance during the wake roll-up. All harmonics attest to the presence of stationary events affecting the flow topology in a way that may locally conceal certain frequencies. Back-scattering of energy to lower frequencies was also observed, as complementary evidence of the intense vortex interaction activity, where small scales also combine to form larger coherent scales.

Despite some simplifications, we believe that our simulations captured most of the relevant physics associated with the roll-up of wakes generated from a rotorcraft, and with the eventual emergence of a 2-VS with turbulence in statistical equilibrium. We finally notice that no significant decay of the wake circulation was observed in the present simulations. Γ_w should however start decreasing further downstream —as it is the case for the turbulent wake of wings— because of exchange of vorticity through the wake mid-plane. In that respect, the interaction of the rotor wake with the fuselage, with the tail rotor, and with the wakes of these elements, would further accelerate the transition to a fully turbulent decaying wake at equilibrium.

ACCEPTED MANUSCRIPT
Physics of Fluids
This is the author's peer reviewed, accepted manuscript. However, the online version of record will be different from this version once it has been copyedited and typeset.
PLEASE CITE THIS ARTICLE AS DOI:10.1063/5.0015162
AIP Publishing

ACKNOWLEDGMENTS

The development work benefited from the computational resources provided by the supercomputing facilities of the Université catholique de Louvain (CISM/UCL) and the Consortium des Équipements de Calcul Intensif (CÉCI) en Fédération Wallonie Bruxelles (FWB) funded by the Fond de la Recherche Scientifique de Belgique (F.R.S.-FNRS) under Convention No. 2.5020.11. The production simulations used computational resources made available on the Tier-1 supercomputer of the FWB, infrastructure funded by the Walloon Region under the Grant Agreement No. 1117545.

DATA AVAILABILITY STATEMENT

The data that support the findings of this study are available from the corresponding author upon reasonable request.

REFERENCES

[1]N. Matayoshi and Y. Okuno, "Evaluation of helicopter encounters with wake vortices," in *35th European Rotorcraft Forum* (2009).

[2]Y. Wang, M. White, G. Barakos, P. Tormey, and P. Pantazopoulou, "Simulation of a Light Aircraft Encountering a Helicopter Wake," Journal of Aircraft **52**, 510–523 (2014).

[3]W. McCroskey, "Vortex wakes of rotorcraft," in *33th Aerospace Sciences Meeting and Exhibit, Reno, NV, January* (1995) pp. 9–12.

[4]S. A. Teager, K. J. Biehl, L. J. Garodz, J. J. Tymczyszym, and D. C. Burnham, "Flight Test Investigation of Rotorcraft Wake Vortices in Forward Flight." Tech. Rep. (Federal Aviation Administration Technical Center, Atlantic City, 1996).

[5]A. Gardner, C. Wolf, and M. Raffel, "Review of measurement techniques for unsteady helicopter rotor flows," Progress in Aerospace Sciences **111**, 100566 (2019).

[6]A. Bauknecht, C. B. Merz, and M. Raffel, "Airborne visualization of helicopter blade tip vortices," Journal of Visualization **20**, 139–150 (2017).

[7]J. G. Leishman, M. J. Bhagwat, and A. Bagai, "Free-vortex filament methods for the analysis of helicopter rotor wakes," Journal of aircraft **39**, 759–775 (2002).

ACCEPTED MANUSCRIPT
Physics of Fluids
This is the author's peer reviewed, accepted manuscript. However, the online version of record will be different from this version once it has been copyedited and typeset.
PLEASE CITE THIS ARTICLE AS DOI:10.1063/5.0015162
AIP Publishing

ACCEPTED MANUSCRIPT
Physics of Fluids
This is the author's peer reviewed, accepted manuscript. However, the online version of record will be different from this version once it has been copyedited and typeset.
PLEASE CITE THIS ARTICLE AS DOI:10.1063/5.0015162
AIP Publishing

[8]N. M. Komerath, M. J. Smith, and C. Tung, "A review of rotor wake physics and modeling," Journal of the American Helicopter Society **56**, 22006–22006 (2011).

[9]N. M. Chaderjian, "Navier-stokes simulation of uh-60a rotor/wake interaction using adaptive mesh refinement," in *73rd AHS International Annual Forum & Technology Display*, ARC-E-DAA-TN40776, edited by A. H. Society (NASA, 2017).

[10]R. Jain, "Sensitivity study of high-fidelity hover predictions on the sikorsky s-76 rotor," Journal of Aircraft **55**, 78–88 (2018), https://doi.org/10.2514/1.C034076.

[11]S. Peron, T. Renaud, I. Mary, C. Benoit, and M. Terracol, "An Immersed Boundary Method for preliminary design aerodynamic studies of complex configurations," in *23rd AIAA Computational Fluid Dynamics Conference* (2017) p. 3623.

[12]Y. T. Delorme, S. H. Frankel, R. Jain, and R. Strawn, "High-order large eddy simulation and immersed boundary method on dynamic meshes: Application to rotorcraft aerodynamics," in *2018 AIAA Aerospace Sciences Meeting* (2018) https://arc.aiaa.org/doi/pdf/10.2514/6.2018-0599.

[13]J. R. Forsythe, E. Lynch, S. Polsky, and P. Spalart, "Coupled flight simulator and cfd calculations of ship airwake using kestrel," in *53rd AIAA Aerospace Sciences Meeting* (2015) p. 0556.

[14]R. Stanly, Y. T. Delorme, and S. H. Frankel, "Computational assessment of actuator line model for large eddy simulation of rotor noise," in *AIAA Scitech 2020 Forum* (2020) https://arc.aiaa.org/doi/pdf/10.2514/6.2020-0035.

[15]J. N. Sorensen and W. Z. Shen, "Numerical modeling of wind turbine wakes," Journal of Fluids Engineering - Transactions of the ASME **124**, 393–399 (2002).

[16]S. Ivanell, J. N. Sorensen, R. Mikkelsen, and D. Henningson, "Analysis of Numerically Generated Wake Structures," Wind Energy **12**, 63–80 (2009).

[17]M. J. Churchfield, S. Schreck, L. A. Martinez-Tossas, C. Meneveau, and P. R. Spalart, "An Advanced Actuator Line Method for Wind Energy Applications and Beyond," in *35th Wind Energy Symposium* (2017) p. 1998.

[18]R. E. Brown and A. J. Line, "Efficient high-resolution wake modeling using the vorticity transport equation," AIAA journal **43**, 1434–1443 (2005).

[19]G. R. Whitehouse and A. H. Boschitsch, "Innovative Grid-Based Vorticity–Velocity Solver for Analysis of Vorticity-Dominated Flows," AIAA Journal **53**, 1655–1669 (2014).

[20]H. W. Kim and R. E. Brown, "A comparison of coaxial and conventional rotor performance," Journal of the American Helicopter Society **55**, 12004 (2010).

[21]P. Singh and P. P. Friedmann, "Application of vortex methods to coaxial rotor wake and load calculations in hover," Journal of Aircraft **55**, 373–381 (2018), https://doi.org/10.2514/1.C034520.

[22]J. Tan and H. Wang, "Simulating unsteady aerodynamics of helicopter rotor with panel/viscous vortex particle method," Aerospace Science and Technology **30**, 255–268 (2013).

[23]J. Tan, Y. Sun, and G. Barakos, "Unsteady loads for coaxial rotors in forward flight computed using a vortex particle method," The Aeronautical Journal **122**, 693–714 (2018).

[24]C. He and N. Rajmohan, "Modeling the Aerodynamic Interaction of Multiple Rotor Vehicles and Compound Rotorcraft with Viscous Vortex Particle Method," in *American Helicopter Society 72nd Annual Forum* (West Palm Beach, 2016).

[25]Y. Shi, Y. Xu, G. Xu, and P. Wei, "A coupling Vwm/Cfd/Csd method for rotor airload prediction," Chinese Journal of Aeronautics **30**, 204–215 (2017).

[26]I. C. Wilbur, A. Moushegian, M. J. Smith, and G. R. Whitehouse, "Uh-60a rotor analysis with an accurate dual-formulation hybrid aeroelastic methodology," Journal of Aircraft , 1–15 (2020), https://doi.org/10.2514/1.C035467.

[27]A. Jimenez-Garcia, G. Barakos, V. Treve, F. Rooseleer, V. Cappellazzo, and R. Graham, "Helicopter wake encounters in the context of RECAT-EU," 43rd European Rotorcraft Forum (2017).

[28]D.-G. Caprace, S. Buffin, M. Duponcheel, P. Chatelain, and G. Winckelmans, "Large Eddy Simulation of Advancing Rotor for Near to Far Wake Assessment," in *43rd European Rotorcraft Forum* (Milan, Italy, 2017) p. 570.

[29]G. Winckelmans, R. Cocle, L. Dufresne, and R. Capart, "Vortex methods and their application to trailing wake vortex simulations," C. R. Phys. **6**, 467–486 (2005).

[30]P. Chatelain, S. Backaert, G. Winckelmans, and S. Kern, "Large eddy simulation of wind turbine wakes," Flow, Turbulence and Combustion **91**, 587–605 (2013).

[31]P. Chatelain, M. Duponcheel, D.-G. Caprace, Y. Marichal, and G. Winckelmans, "Vortex particle-mesh simulations of vertical axis wind turbine flows: from the airfoil performance to the very far wake," Wind Energy Science **2**, 317 (2017).

[32]P. Chatelain, M. Duponcheel, S. Zeoli, S. Buffin, D.-G. Caprace, G. Winckelmans, and L. Bricteux, "Investigation of the effect of inflow turbulence on vertical axis wind turbine wakes," Journal of Physics: Conference Series **854**, 012011 (2017).

[33]R. Cocle, G. Winckelmans, and G. Daeninck, "Combining the vortex-in-cell and parallel fast multipole methods for efficient domain decomposition simulations," Journal of Computational Physics **227**, 9091–9120 (2008).

ACCEPTED MANUSCRIPT
Physics of Fluids
This is the author's peer reviewed, accepted manuscript. However, the online version of record will be different from this version once it has been copyedited and typeset.
PLEASE CITE THIS ARTICLE AS DOI:10.1063/5.0015162
AIP Publishing

[34]G.-H. Cottet and P. Koumoutsakos, *Vortex Methods, Theory and Practice* (Cambridge University Press, 2000).

[35]G. S. Winckelmans, "Encyclopedia of Computational Mechanics," (John Wiley & Sons, Ltd, 2004) Chap. Vortex Methods, pp. 129–153.

[36]P. Chatelain, A. Curioni, M. Bergdorf, D. Rossinelli, W. Andreoni, and P. Koumoutsakos, "Billion vortex particle Direct Numerical Simulations of aircraft wakes," Computer Methods in Applied Mechanics and Engineering **197**, 1296–1304 (2008).

[37]I. F. Sbalzarini, J. H. Walther, M. Bergdorf, S. E. Hieber, E. M. Kotsalis, and P. Koumoutsakos, "PPM A highly efficient parallel particle mesh library for the simulation of continuum systems," J. Comput. Phys. **215**, 566–588 (2006).

[38]P. Chatelain and P. Koumoutsakos, "A Fourier-based elliptic solver for vortical flows with periodic and unbounded directions," Journal of Computational Physics **229**, 2425–2431 (2010).

[39]D.-G. Caprace, T. Gillis, and P. Chatelain, "FLUPS - a fourier-based library of unbounded poisson solvers," submitted to SIAM Journal on Scientific Computing (2019).

[40]D.-G. Caprace, G. Winckelmans, and P. Chatelain, "An immersed lifting and dragging line model for the large eddy simulation of wake flows," Theoretical and Computational Fluid Dynamics **34**, 21–48 (2020).

[41]E. Dyachuk, A. Goude, and H. Bernhoff, "Dynamic stall modeling for the conditions of vertical axis wind turbines," AIAA journal **52**, 72–81 (2013).

[42]D.-G. Caprace, P. Chatelain, and G. Winckelmans, "Lifting line with various mollifications: Theory and application to an elliptical wing," AIAA Journal **57**, 1–12 (2019).

[43]A. R. Meyer Forsting, G. R. Pirrung, and N. Ramos-García, "A vortex-based tip/smearing correction for the actuator line," Wind Energy Science (2019), 10.5194/wes-2018-76.

[44]N. Docquier, A. Poncelet, and P. Fisette, "Robotran: a powerful symbolic generator of multibody models," Mechanical Sciences **4**, 199–219 (2013).

[45]B. Berry and I. Chopra, "Wind Tunnel Testing of an Instrumented Rotor at High Advance Ratio," in *56th AIAA/ASCE/AHS/ASC Structures, Structural Dynamics, and Materials Conference* (2015).

[46]G. M. Bowen-Davies, *Performance and Loads of Variable Tip Speed Rotorcraft at High Advance Ratios*, Ph.D. thesis, University of Maryland, College Park (2015).

[47]A. H. Lind and A. R. Jones, "Unsteady airloads on static airfoils through high angles of attack and in reverse flow," Journal of Fluids and Structures **63**, 259–279 (2016).

ACCEPTED MANUSCRIPT
Physics of Fluids
This is the author's peer reviewed, accepted manuscript. However, the online version of record will be different from this version once it has been copyedited and typeset.
PLEASE CITE THIS ARTICLE AS DOI:10.1063/5.0015162
AIP Publishing

[48]G. Bir, I. Chopra, and K. Nguyen, "Development of UmaRc (University of Maryland Advanced Rotorcraft Code)," in *American Helicopter Society 46th Annual Forum* (1990).

[49]M. Shives and C. Crawford, "Mesh and load distribution requirements for actuator line cfd simulations," Wind Energy **16**, 1183–1196 (2013).

[50]K. S. Wittmer, W. J. Devenport, M. C. Rife, and S. A. Glegg, "Perpendicular blade vortex interaction," AIAA journal **33**, 1667–1674 (1995).

[51]D. J. Garmann and M. R. Visbal, "Interactions of a streamwise-oriented vortex with a finite wing," Journal of Fluid Mechanics **767**, 782–810 (2015).

[52]D. Reich, S. Willits, and S. Schmitz, "Scaling and Configuration Effects on Helicopter Rotor Hub Interactional Aerodynamics," Journal of Aircraft (2017), 10.2514/1.C034250.

[53]F. Noca, D. Shiels, and D. Jeon, "A comparison of methods for evaluating time-dependent fluid dynamic forces on bodies, using only velocity fields and their derivatives," Journal of Fluids and Structures **13**, 551–578 (1999).

[54]J. G. Leishman, *Principles of helicopter aerodynamics*, 2nd ed. (Cambridge University Press, 2006).

[55]I. De Visscher, L. Bricteux, and G. Winckelmans, "Aircraft vortices in stably stratified and weakly turbulent atmospheres: simulation and modeling," AIAA Journal **51** (2013), 10.2514/1.J051742.

[56]I. De Visscher, *Interaction of wake vortices with the atmosphere and the ground : advanced numerical simulation and operational modeling*, Ph.D. thesis, Université catholique de Louvain (2012).

[57]D. A. Kovalev, D. Vanhoenacker-Janvier, P. Billuart, M. Duponcheel, and G. Winckelmans, "Modeling of wake vortex radar detection in clear air using large-eddy simulation," Journal of Atmospheric and Oceanic Technology **36**, 2045–2062 (2019), https://doi.org/10.1175/JTECH-D-18-0127.1.

[58]C. Breitsamter, "Wake vortex characteristics of transport aircraft," Progress in Aerospace Sciences **47**, 89 – 134 (2011).

ACCEPTED MANUSCRIPT
Physics of Fluids
This is the author's peer reviewed, accepted manuscript. However, the online version of record will be different from this version once it has been copyedited and typeset.
PLEASE CITE THIS ARTICLE AS DOI:10.1063/5.0015162
AIP Publishing